

RESEARCH ARTICLE

Rac1, the actin cytoskeleton and microtubules are key players in clathrin-independent endophilin-A3-mediated endocytosis

François Tyckaert^{1,2}, Natacha Zanin², Pierre Morsomme^{1,*} and Henri-François Renard^{2,*}

ABSTRACT

Endocytic mechanisms actively regulate plasma membrane composition and sustain fundamental cellular functions. Recently, we identified a clathrin-independent endocytic (CIE) modality mediated by the BAR domain protein endophilin-A3 (endoA3, encoded by *SH3GL3*), which controls the cell surface homeostasis of the tumor marker CD166 (also known as ALCAM). Deciphering the molecular machinery of endoA3-dependent CIE should therefore contribute to a better understanding of its pathophysiological role, which remains so far unknown. Here, we investigate the role of actin, Rho GTPases and microtubules, which are major players in CIE processes, in this mechanism. We show that the actin cytoskeleton is dynamically associated with endoA3- and CD166-positive endocytic carriers, and that its perturbation strongly inhibits the process of CD166 uptake. We also reveal that the Rho GTPase Rac1, but not Cdc42, is a master regulator of this endocytic route. Finally, we provide evidence that microtubules and kinesin molecular motors are required to potentiate endoA3-dependent endocytosis. Of note, our study also highlights potential compensation phenomena between endoA3-dependent CIE and macropinocytosis. Altogether, our data deepen our understanding of this CIE modality and further differentiate it from other unconventional endocytic mechanisms.

This article has an associated First Person interview with the first author of the paper.

KEY WORDS: CD166, Endocytosis, Actin, Microtubule, Endophilin

INTRODUCTION

CD166 (also termed ALCAM for ‘activated leukocyte cell adhesion molecule’) is a cell surface transmembrane glycoprotein that belongs to a small subgroup of the immunoglobulin superfamily (IgSF). This protein acts as a cell-cell adhesion molecule via homophilic (CD166–CD166) or heterophilic (CD166–CD6) interactions between adjacent cells (Ferragut et al., 2021). Heterophilic interactions are particularly important at the immune synapse, where CD166 is exposed at the cell surface of antigen-presenting cells and can interact with its ligand CD6 expressed at the surface of T cells (Zimmerman et al., 2006). Given its broad tissue distribution,

CD166 is involved in cellular processes as diverse as neuronal growth (Bye et al., 2019; Pollerberg et al., 2013), hematopoiesis (Chitteti et al., 2014; Ohneda et al., 2001), cell migration (Cayrol et al., 2008; Willrodt et al., 2019) and T cell activation (Hassan et al., 2004; Zimmerman et al., 2006). More importantly, CD166 is dysregulated in various types of tumors (e.g. pancreatic and colorectal cancers) in which its high protein expression level often correlates with poor prognosis (Kahlert et al., 2009; Munsterberg et al., 2020; Sanders et al., 2019; Zhang et al., 2017).

Recently, we have shown that CD166 is endocytosed through a clathrin-independent endocytic (CIE) modality controlled by the Bin/Amphiphysin/Rvs (BAR) domain protein endophilin-A3 (endoA3, encoded by *SH3GL3*) and galectin-8 (Renard et al., 2020). In this mechanism, distinct from the previously described fast endophilin-mediated endocytosis (FEME) (Boucrot et al., 2015), extracellular galectin-8 is thought to cluster glycosylated CD166 as well as glycosphingolipids to initiate plasma membrane deformation, according to the glycolipid-lectin (GL-Lect) hypothesis (Johannes et al., 2016). The current model hypothesizes that clustering of CD166 molecules is followed by the recruitment of endoA3, which further increases plasma membrane curvature to form endocytic carriers. Strikingly, we have previously demonstrated that this endocytic modality allows the fine-tuning of CD166 molecules at the surface of some cancer cells, directly modulating intercellular adhesiveness as well as ensuring optimal collective migration (Renard et al., 2020). Still, further characterization of the molecular players as well as more insight into their coordination will help to better understand the physiological role of this endocytic modality, especially in the context of cancer.

As previously described by Nelissen et al. (2000), CD166 organization at the plasma membrane is highly modulated by the actin cytoskeleton, which is crucial for the assembly of strong and stable cell adhesion complexes. Of note, actin polymerization contributes to the formation and scission of many CIE carriers (Boucrot et al., 2015; Renard et al., 2015), modulating membrane tension at the site of invagination (Boulant et al., 2011) and providing pulling forces through myosin-based motor activity (Kumari et al., 2019; Soriano-Castell et al., 2017). Small Rho GTPases, such as RhoA, Rac1 and Cdc42, actively regulate actin dynamics in CIE mechanisms. For instance, Cdc42 is the main regulator of clathrin-independent carriers/GPI-anchored protein enriched early endosomal compartment (CLIC/GEEC) endocytosis (Rossatti et al., 2019), whereas RhoA and Rac1 regulate the internalization of IL2Rβ (Grassart et al., 2008). FEME requires all three Rho GTPases, with Cdc42 acting as the key regulator of the FEME priming complex (Boucrot et al., 2015; Chan Wah Hak et al., 2018). Finally, it is worth mentioning that macropinocytosis is highly dependent on Rac1 activation (Egami et al., 2014).

In addition to the actin cytoskeleton, a number of studies have highlighted the ability of microtubules to deform membranes (Day et al., 2015), as well as to mediate scission during CIE (Ferreira et al.,

¹UCLouvain, Louvain Institute of Biomolecular Science and Technology (LIBST), Group of Molecular Physiology, Croix du Sud 4-5, B-1348 Louvain-la-Neuve, Belgium. ²UNamur, NARILIS, Unité de Recherche en Biologie Cellulaire animale (URBC), Rue de Bruxelles 61, B-5000 Namur, Belgium.

*Authors for correspondence (henri-francois.renard@unamur.be; pierre.morsomme@uclouvain.be)

DOI: 10.1242/jcs.259623; N.Z., 0000-0002-3062-3036; P.M., 0000-0001-7780-7230; H.-F.R., 0000-0002-2406-2519

2021; Renard et al., 2015; Simunovic et al., 2017). In both cases, the presence of a pulling force is required and provided by microtubule-based motors, comprising two classes of motor proteins – dyneins and kinesins. Whereas plus-end kinesins can deform giant unilamellar vesicles (GUVs) *in vitro* (Leduc et al., 2004), the minus-end directed motor dynein proved to be the main driving force during endocytosis (Ferreira et al., 2021) given the preferential growth of plasma membrane invaginations towards the cell center. Minus-end directed kinesin-14 members might also contribute to endocytosis, although these proteins are mainly associated with mitotic spindle assembly and vesicle transport (Loncar et al., 2020; Noda et al., 2001; Yang and Sperry, 2003). In the context of CIE, microtubule-based scission requires the synergic action of the actin cytoskeleton, dynamin, dynein and a membrane-bound protein scaffold (e.g. a BAR domain protein) imposing frictional forces onto the membrane (Simunovic et al., 2017). This so-called friction-driven scission (FDS) mechanism has been described to mediate the scission of bacterial toxin-induced plasma membrane invaginations (Renard et al., 2015) and FEME carriers (Boucrot et al., 2015; Ferreira et al., 2021), with endophilin-A2 providing the scaffold that generates friction.

In this study, we investigate the role of the actin cytoskeleton, small Rho GTPases and microtubules in the endoA3-dependent endocytosis of CD166. To do so, we performed a molecular screen using various inhibitors and siRNAs against components of the actin and microtubule cytoskeleton, and systematically looked for functional effects by monitoring CD166 uptake. Functional data were achieved by colocalization experiments in order to visualize whether these molecular players are physically associated with

CD166-containing endocytic carriers. Using this strategy, we show that the actin cytoskeleton is dynamically associated with CD166 endocytic carriers and that its disruption strongly inhibits endoA3-dependent uptake of CD166. In addition, the actin-dependent molecular motor non-muscle myosin 2A (heavy chain encoded by *MYH9*), which has been recently shown to act in the CIE of MHC class I molecules (MHCI) (Wayt et al., 2021), is a crucial effector of endoA3-dependent uptake of CD166. We also demonstrate that the small Rho GTPase Rac1, but not Cdc42, modulates the function of actin in this process. Finally, we provide a strong body of evidence that microtubules and kinesin molecular motors are required to potentiate endoA3-dependent CIE, most likely through an FDS mechanism, similar to that proposed for endoA2-mediated CIE of bacterial toxins (Renard et al., 2015; Simunovic et al., 2017) and FEME (Ferreira et al., 2021). While our study identifies new molecular players involved in the endoA3-dependent CIE modality, the data also further distinguish this mechanism from other unconventional endocytic processes such as macropinocytosis, FEME or CLIC/GEEC endocytosis. Strikingly, our data also point out potential compensation phenomena occurring between endoA3-dependent CIE and macropinocytosis.

RESULTS

The actin cytoskeleton dynamically associates with endoA3-dependent CIE machinery

Super resolution observation of HeLa cells by Airyscan confocal microscopy revealed a strong association of CD166- and endoA3-positive endocytic structures with F-actin (Fig. 1A, left panel).

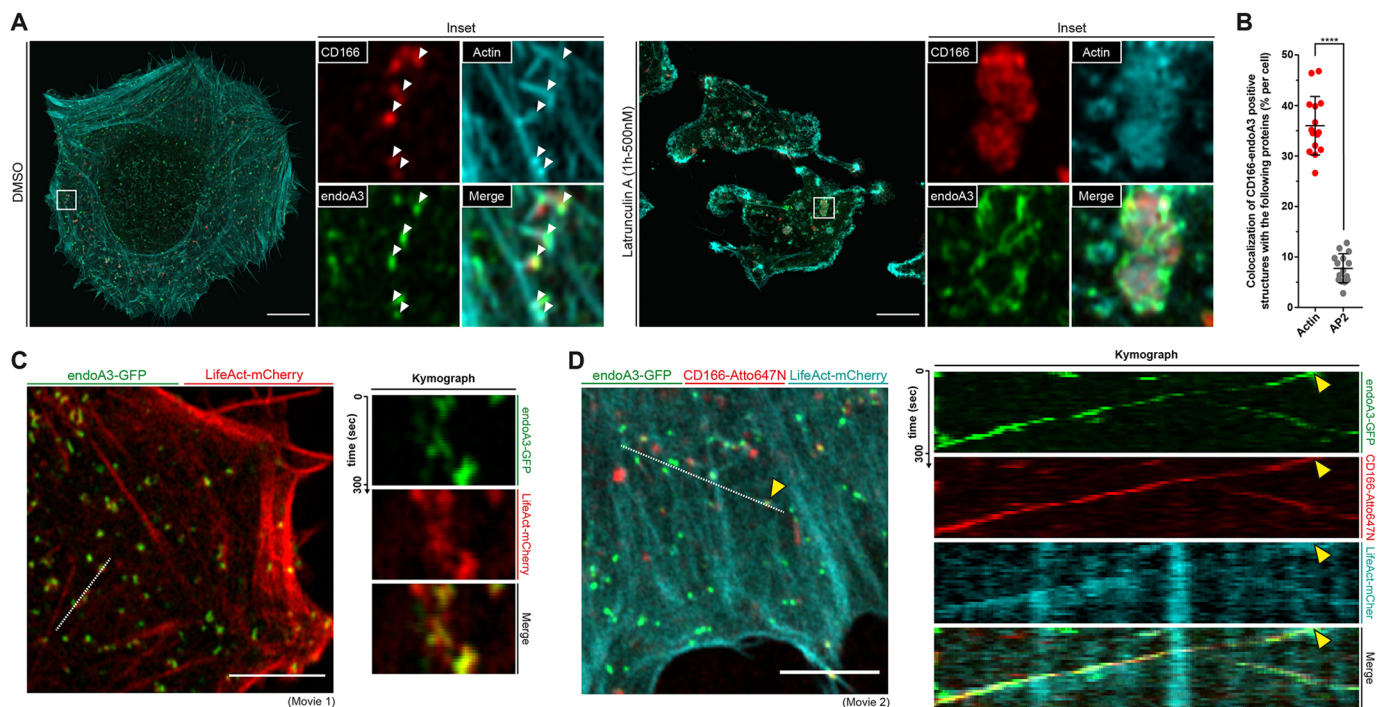


Fig. 1. Actin cytoskeleton dynamically associates with endoA3-dependent CIE machinery. (A) Continuous anti-CD166 antibody uptake (red, Atto647N) in HeLa cells stably expressing GFP-tagged endophilin-A3 (green) and treated for 1 h with DMSO (left panel) or 500 nM latrunculin-A (right panel). Cells were fixed and stained for the actin cytoskeleton with fluorescently labeled phalloidin (cyan, Alexa Fluor 555). Images representative of three independent experiments. White arrowheads indicate colocalization events. (B) Quantification of colocalization between CD166–endoA3-positive structures and actin (from A, DMSO condition) or the mCherry-tagged $\mu 2$ subunit of the AP2 complex (negative control, representative image in Fig. S1A). $n=15$ cells, three independent experiments. **** $P<0.0001$ (one-way ANOVA with Sidak's multiple comparison test). Error bars are mean \pm s.e.m. (C,D) Live acquisitions of HeLa cells stably expressing GFP-tagged endoA3 and transfected with LifeAct–mCherry captured by Airyscan confocal microscopy in the absence (C) or presence (D) of fluorescently labeled anti-CD166 antibody (Atto647N). Kymographs illustrate the dynamic association of endoA3 with actin (C) and their strong association with CD166 endocytic carriers (yellow arrowhead in D). The dashed line indicates kymograph origins. Images are extracted from time series of 30 frames, with a 10 s interval between each frame (Movies 1, 2, respectively). Images representative of three independent experiments. Scale bars: 10 μ m (A), 5 μ m (C,D).

When cells were treated with latrunculin A, an inhibitor of actin polymerization, membranous CD166 relocated in dense actin clusters (Fig. 1A, right panel). This observation is consistent with previous studies showing that the disruption of the actin cytoskeleton with cytochalasin D results in an increased lateral mobility of the protein and in the formation of high avidity CD166 clusters (Nelissen et al., 2000; Zimmerman et al., 2004). Interestingly, endoA3 also relocated at the edge of these actin-rich CD166 clusters, further highlighting the strong association between the three partners. Quantification of this association in the DMSO condition revealed that 36% of CD166–endoA3-positive structures colocalize with actin (Fig. 1B), unlike the clathrin adaptor complex AP2 (8%), used here as a negative control (representative image in Fig. S1A). Confocal live-cell imaging provided a more dynamic view of GFP-tagged endoA3 association with the actin cytoskeleton, as revealed with LifeAct–mCherry (Fig. 1C; Movie 1). Remarkably, the appearance of an endoA3-positive spot at the cell surface was systematically escorted by a local actin enrichment (Fig. 1C). These observations are reminiscent of the dynamic co-distribution previously documented between endoA2 and actin, notably in the context of CIE of bacterial toxins (Renard et al., 2015) and FEME (Boucrot et al., 2015). Additionally, the tracking of fluorescently labeled anti-CD166 antibody revealed endocytic structures simultaneously positive for both CD166 and endoA3, moving along with actin (Fig. 1D, yellow arrow; Movie 2). Altogether, these data highlight the dynamic and specific association of the endoA3-dependent endocytic machinery with the actin cytoskeleton.

Disruption of the actomyosin cytoskeleton impairs CD166 uptake

Next, we aimed to assess the functional consequences of this dynamic association between the actin cytoskeleton and endoA3-dependent CIE. To do so, we measured the uptake of the cargo CD166 upon acute impairment of actin polymerization using several drugs (Fig. 2A; representative images in Fig. S2A). Consistently, the inhibition of actin polymerization by latrunculin A, cytochalasin D and the ARP2/3 complex inhibitor CK-666 (Coué et al., 1987; Schliwa, 1982; Nolen et al., 2009) drastically reduced CD166 uptake (Fig. 2A, left panel). Of note, the most potent effect on CD166 uptake was obtained with jasplakinolide, a strong inhibitor of actin depolymerization (Bubb et al., 2000). In addition, we focused on the role of ezrin, which has been demonstrated to interact directly with CD166 and to connect it to the actin cytoskeleton (Tudor et al., 2014). Interestingly, an acute treatment with the ezrin inhibitor NSC668394 (Bulut et al., 2012) resulted in a significant decrease of CD166 endocytosis by 50%, which is similar to the effect observed with cytochalasin D or CK-666 drugs (Fig. 2A, left panel). On the other hand, actin disruption with the previous inhibitors had little to no effect on transferrin (Tf) uptake, used here as a marker of the canonical clathrin-mediated endocytosis (CME) (Fig. 2A, right panel). This observation is consistent with previous reports showing that actin is less crucial in mediating functional CME in animal cells (Boucrot et al., 2015; Fujimoto et al., 2000), although this can be dependent on the cell type and the size of the cargo (Mooren et al., 2012). As an alternative to molecular inhibitors, we also performed CD166 and Tf uptake assays in cells treated with siRNAs against the ARP2/3 complex subunit 2 (ARPC2) (Fig. 2B; representative images in Fig. S2B). As for the ARP2/3 inhibitor CK-666, ARPC2 depletion led to a reduction of CD166 uptake (–42%) (Fig. 2B, left panel), while no effect was observed on Tf uptake (Fig. 2B, right panel). Of note, total internal reflection fluorescence (TIRF) live-cell imaging

showed that ARPC2 dynamically co-distributes with endoA3 at the plasma membrane (Fig. 2C; Movie 3), as observed above with actin (Fig. 1C).

Contractile forces generated by myosin motors moving along F-actin filaments actively regulate the remodeling and dynamics of the actin cytoskeleton. This so-called actomyosin cytoskeleton has been recently shown to participate in several CIE mechanisms (Soriano-Castell et al., 2017; Wayt et al., 2021; Williamson and Donaldson, 2019). More specifically, non-muscle myosin 2A and 2B isoforms (heavy chains encoded by *MYH9* and *MYH10*, respectively; hereafter referred to as myosin 2 isoforms or proteins) were shown to drive the internalization of distinct CIE cargoes, MHCI and CD59, respectively, presumably by regulating actin contractility and membrane tension at the invagination site (Wayt et al., 2021). To test whether myosin 2 isoforms have a similar function during CD166 endocytosis, we treated cells with blebbistatin, a selective inhibitor of myosin 2 proteins (Fig. 2D; representative images in Fig. S2C). Interestingly, blebbistatin reduced the uptake of CD166 in a time-dependent manner (Fig. 2D, left panel), as opposed to what was observed with the CME cargo Tf (Fig. 2D, right panel). An siRNA-based depletion of each myosin 2 isoform revealed a specific role of myosin 2A in the uptake of CD166 (Fig. 2E; representative images in Fig. S2D), which is reminiscent of the effect on MHCI internalization (Wayt et al., 2021). In addition, partial colocalization between CD166–endoA3-positive structures and myosin 2A could be observed (23%, Fig. 2F), when compared to myosin 2B (15%, Fig. 2F; representative image in Fig. S1A) or the clathrin adaptor complex AP2 (8%, negative control, Fig. 2F; representative image in Fig. S1A). This observation suggests a function for myosin 2A at CD166 uptake sites that is probably transient. Alternatively, myosin 2A might also regulate actin contractility and membrane tension further from uptake sites, as proposed for MHCI (Wayt et al., 2021). Of note, although myosin 2A depletion does have a strong effect on CD166 and MHCI uptake, MHCI internalization is not affected by the depletion of any of the endoA isoforms (Fig. S1B), indicating that both cargoes are endocytosed through distinct CIE mechanisms. Collectively, these results highlight the functional implication of the actin cytoskeleton and myosin 2A in the endoA3-dependent CIE of CD166.

Rac1 – but not Cdc42 – regulates endoA3-mediated CIE

In light of the crucial role of actin dynamics in the endoA3-mediated CIE of CD166, we next focused on the role of small Rho GTPases that could regulate the process. First, we measured the uptake of CD166 cargo in cells transiently expressing GFP-tagged Rac1 or Cdc42 GTPases under their wild-type (WT), dominant-negative (Rac1^{N17} and Cdc42^{N17} mutants) or constitutively active (Rac1^{V12} and Cdc42^{L61}) forms (Fig. 3A,B; representative images in Fig. S3A,B). Strikingly, the expression of Rac1^{N17} dominant-negative mutant reduced the uptake of CD166 by 42% as compared to control cells expressing free GFP only (Fig. 3A). By contrast, the expression of WT and Rac1^{V12} resulted in a strong increase in endocytosis by 82% and 187%, respectively (Fig. 3A). Regarding Cdc42, the expression of the WT form as well as the dominant-negative mutant Cdc42^{N17} did not alter CD166 uptake (Fig. 3B). Intriguingly, the expression of the constitutively active mutant Cdc42^{L61} resulted in a sharp increase of CD166 endocytosis by 159%, as observed for Rac1^{V12}. These results obtained on CD166 uptake with the constitutively active mutants of Rac1 and Cdc42 likely depict non-specific effects, due to the global actin remodeling they prime. Nevertheless, the results obtained with the WT

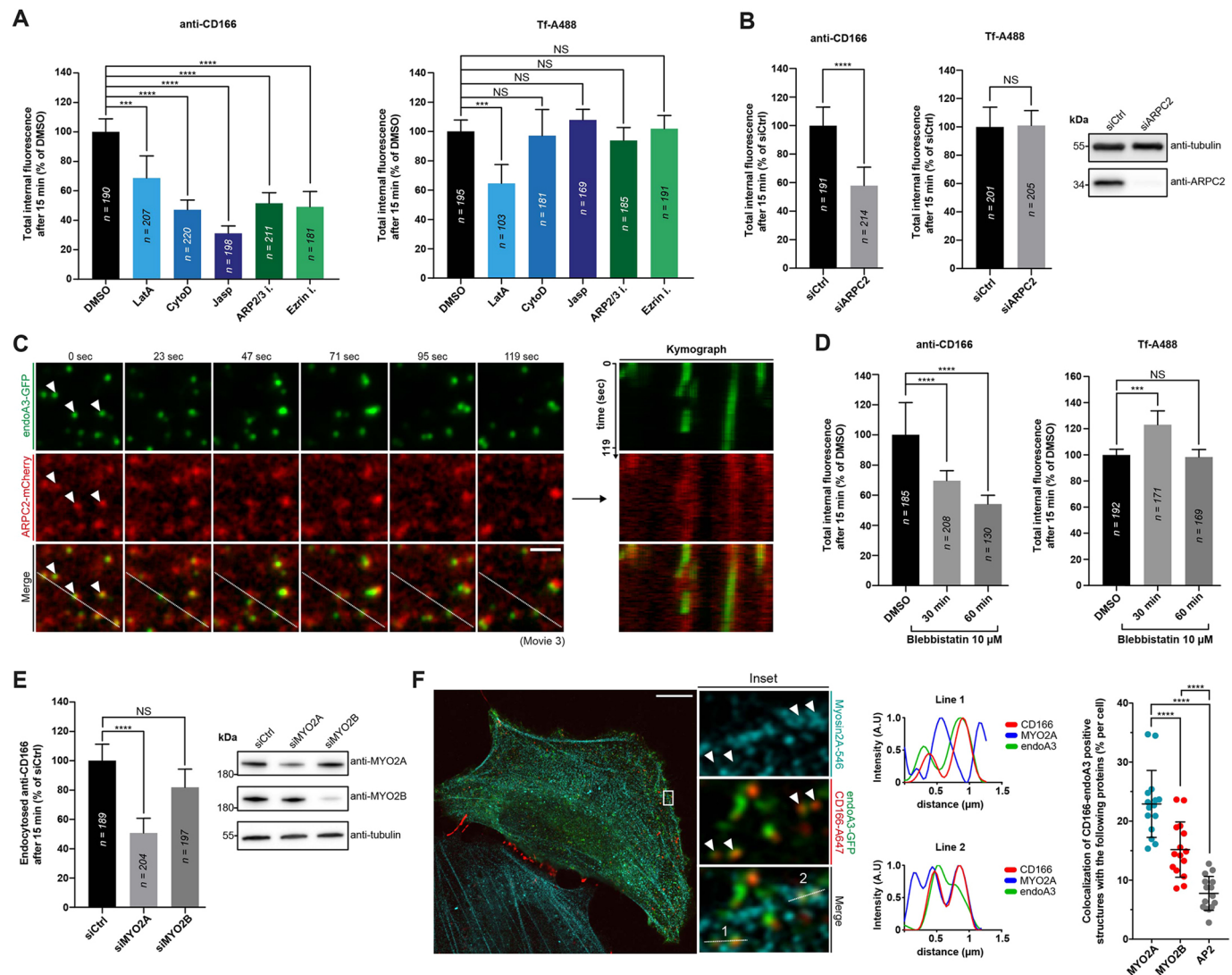


Fig. 2. Inhibition of the actin cytoskeleton and myosin 2A impairs CD166 uptake. (A,B,D,E) Continuous uptake of anti-CD166 antibody or Alexa Fluor 488-labeled transferrin (Tf-A488) for 15 min in HeLa cells. The remaining signal at the cell surface was stripped by acid washes on ice. Internal fluorescence was quantified from confocal images and plotted as the relative percentage of the control condition: DMSO for A and D, and negative control siRNA (siCtrl) for B and E. *n* cells, three independent experiments. NS, not significant; ****P*<0.001, *****P*<0.0001 (A,D,E, Kruskal–Wallis test with Dunn’s multiple comparison post hoc test, two-sided; B, two-tailed unpaired Mann–Whitney *t*-test). Error bars are median with 95% c.i. (A) CD166 and Tf uptake in cells pre-incubated for 1 h with inhibitors of actin polymerization [500 nM latrunculin A (LatA), 100 nM cytochalasin D (CytoD) or 200 nM jasplakinolide (Jasp)] and of ARP2/3 complex (50 μM CK-666; ARP2/3 I.), or pre-incubated for 5 h with ezrin inhibitor (10 μM NSC668394; Ezrin I.). (B) CD166 and Tf uptake in cells transfected with control siRNA (siCtrl) and siRNAs against endogenous ARPC2 (siARPC2). (C) TIRF live-cell imaging of HeLa cells transiently expressing mCherry-tagged ARPC2 and GFP-tagged endoA3. The dashed line indicates kymograph origins. Images are extracted from time series of 61 frames, with a 2.39 s interval between each frame (see Movie 3). White arrowheads indicate colocalizing spots. Representative of ten different time-series acquisitions (two independent experiments). (D) CD166 and Tf uptake in cells pre-incubated for 30 min and 1 h with the myosin 2 inhibitor blebbistatin at 10 μM. (E) CD166 uptake in cells transfected with siRNAs against endogenous myosin 2A and 2B isoforms. (F) Myosin 2A labeling and continuous anti-CD166 uptake in HeLa cells stably expressing GFP-tagged endophilin-A3. Representative of three independent experiments. Note the partial colocalization of CD166–endoA3-positive structures with myosin 2A, as highlighted by the fluorescence profiles and white arrowheads. The graph shows quantification of colocalization between CD166–endoA3-positive structures and endogenous myosin 2 isoforms or mCherry-tagged AP2 complex (negative control) (representative images in Fig. S1A). *n*=15 cells, three independent experiments. *****P*<0.0001 (one-way ANOVA with Sidak’s multiple comparison test). Error bars are mean±s.e.m. Western blots in B and E highlight knockdown efficiency. Scale bars: 2 μm (C), 10 μm (F).

Rho GTPases and their dominant-negative mutants point out a preponderant role of Rac1 in the endocytosis of CD166.

To test this hypothesis more thoroughly, we disturbed the function of these Rho GTPases either by RNA interference (Fig. 3C; representative images in Fig. S3C) or by using a small-molecular inhibitor (Fig. 3D; representative images in Fig. S3D). Remarkably, siRNA depletion of Rac1 reduced the endocytosis of CD166 by 51%, whereas no significant effect was observed upon Cdc42

depletion (Fig. 3C). Furthermore, we focused on Tiam1, a specific guanine-nucleotide exchange factor (GEF) of Rac1 that has been shown to interact with endoA3, leading to the activation of the small GTPase (Poudel et al., 2018). Although displaying a weaker effect than the direct depletion of Rac1, the knockdown of Tiam1 induced a significant reduction of CD166 uptake by 30% (Fig. 3C). This observation suggests that additional unidentified GEFs might account for residual Rac1 activation during CD166 endocytosis.

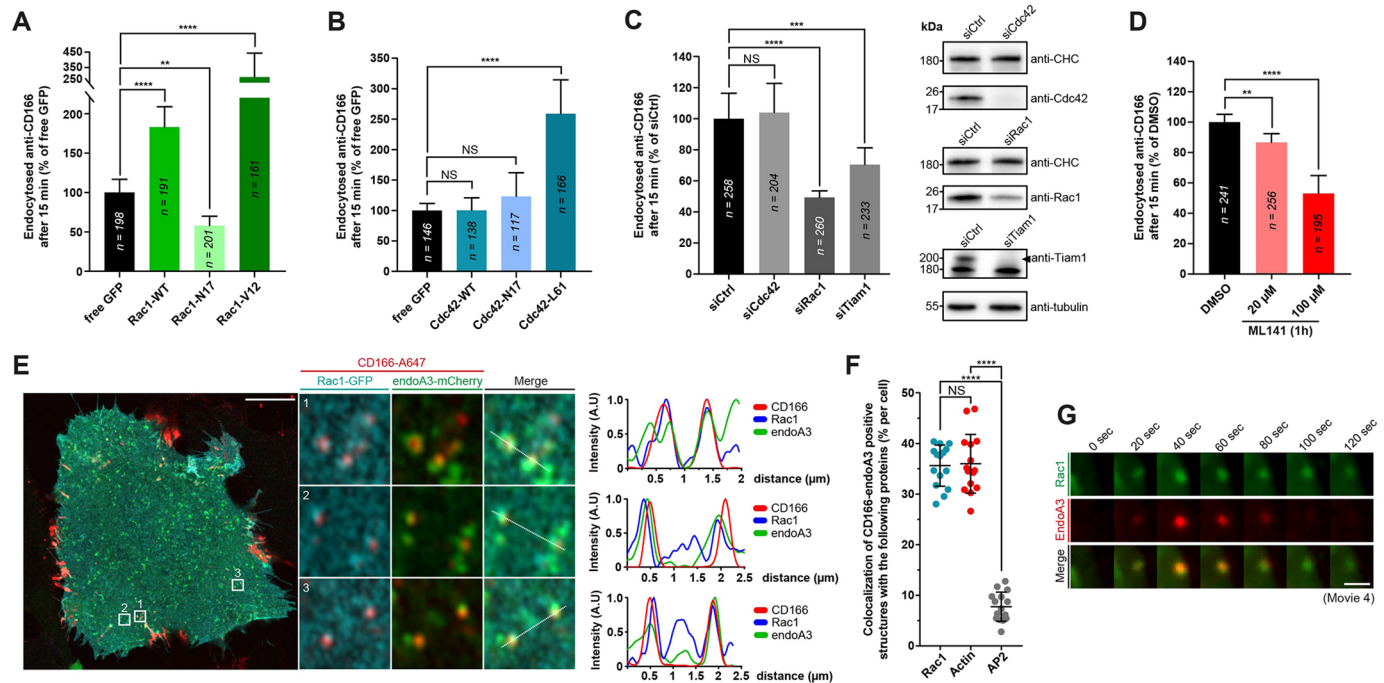


Fig. 3. Rac1, but not Cdc42, regulates the clathrin-independent uptake of CD166. (A–D) Continuous uptake of anti-CD166 antibody for 15 min in HeLa cells. The remaining CD166 signal at the cell surface was stripped by acid washes on ice. Internal fluorescence was quantified from confocal images and plotted as the relative percentage of the control condition: free GFP for A and B, negative control siRNA (siCtrl) for C, and DMSO for D. *n* cells, three independent experiments. NS, not significant. ***P*<0.01, ****P*<0.001, *****P*<0.0001 (Kruskal–Wallis test with Dunn’s multiple comparison post hoc test, two-sided). Error bars are median with 95% c.i. (A,B) CD166 uptake in cells transiently expressing GFP-tagged Rac1 or Cdc42 GTPases under their wild-type (WT), dominant negative (Rac1N17 and Cdc42N17 mutants) or constitutively active (Rac1V12 and Cdc42L61) forms. (C) CD166 uptake in cells transfected with siRNAs against endogenous Cdc42, Rac1 and Tiam1. Western blots show knockdown efficiency. (D) CD166 uptake in cells pre-incubated for 1 h with the indicated concentration of ML141. (E) Continuous anti-CD166 uptake in HeLa cells co-transfected with endoA3–mCherry and Rac1–GFP constructs. Representative of three independent experiments. Note the association of both endoA3 and Rac1 with CD166-positive puncta, as highlighted by the fluorescence profiles. (F) Quantification of colocalization between CD166–endoA3-positive structures and GFP-tagged Rac1 (image in Fig. 3E), actin (image in Fig. 1A) or the mCherry-tagged μ 2 subunit of the AP2 complex (negative control, image in Fig. S1A). *n*=15 cells, three independent experiments (one-way ANOVA with Sidak’s multiple comparison test). Error bars are mean \pm s.e.m. (G) Live TIRF imaging. Time series of an isolated event at plasma membrane, showing dynamic codistribution of GFP-tagged Rac1 and mCherry-tagged endoA3 (related to Fig. S4A, white arrow, and Movie 4). Scale bar: 10 μ m (E), 500 nm (G).

Next, we explored the function of these Rho GTPases by acute treatment of cells with ML141, a selective and reversible non-competitive inhibitor displaying nanomolar potency against Cdc42 (IC₅₀=200 nM), but high micromolar potency against Rac1 (IC₅₀=100 μ M) *in vitro* (Surviladze et al., 2010). Very interestingly, low micromolar doses of ML141 (20 μ M), thought to mainly inhibit Cdc42 but not Rac1, displayed only mild effects on CD166 endocytosis (Fig. 3D). By contrast, high micromolar doses of ML141 (100 μ M), the point at which Rac1 starts to be inhibited, led to a drastic 50% reduction of CD166 uptake (Fig. 3D), in line with the above data obtained upon Rac1-specific inhibition by the expression of a dominant-negative mutant (Fig. 3A) or by RNA interference (Fig. 3C). Accordingly, we could clearly observe triple colocalization events between Rac1, endoA3 and CD166, highlighting their association in the machinery (Fig. 3E). More precisely, 35% of CD166–endoA3 spots associated with Rac1, which, remarkably, is very similar to colocalization levels with actin (36%, Fig. 3F). The dynamic association between endoA3 and Rac1 at the cell surface was further confirmed by TIRF imaging on living cells (Fig. 3G; Fig. S4A, Movie 4). Since Rac1 is known to stimulate ARP2/3-mediated actin branching via its interaction with WAVE proteins, we looked at WASF2 (WAVE isoform 2) distribution at plasma membrane by TIRF live-cell microscopy. In addition to a colocalization with endoA3, WASF2 overexpression led to a stabilization of endoA3 clusters at plasma membrane (Fig. S4B, Movie 5), which is even more apparent when compared

to non-transfected cells (Movie 6). Strikingly, this stabilization of endoA3 at cell surface in WASF2-overexpressing cells correlated with a decrease (–65%) of CD166 uptake (Fig. S4C). This effect might result from reduced membrane deformability, as WASF2 overexpression has been shown to induce the formation of extremely dense actin meshworks presumably increasing cell surface tension (Graziano et al., 2019; Xia et al., 2019). Overall, the data obtained with the expression of Rho GTPase mutants, RNA interference or small-molecule inhibitor treatment converge, indicating a prominent role of Rac1 in endoA3-mediated CIE, rather than Cdc42.

EndoA3-mediated CIE is distinct from macropinocytosis, FEME and CLIC/GEEC endocytosis

To explore the possibility that CD166 is endocytosed through other Rac1-mediated CIE mechanisms, such as macropinocytosis or FEME, we incubated cells with ethylisopropyl amiloride (EIPA), a strong inhibitor of both processes (Boucrot et al., 2015; Koivusalo et al., 2010), and monitored CD166 internalization. Surprisingly, the treatment with EIPA led to a significant increase of CD166 uptake (+60%), with a clear burst of endocytic carriers at the cell periphery (Fig. 4A; representative images in Fig. S4D). Similarly, treatment with EIPA resulted in an increased peripheral distribution of endoA3 (Fig. 4B) and endoA3-positive bursts colocalizing with CD166 endocytic carriers (Fig. 4C). Of note, depletion of Rac1 or endoA3 in EIPA-treated cells led to an almost complete inhibition

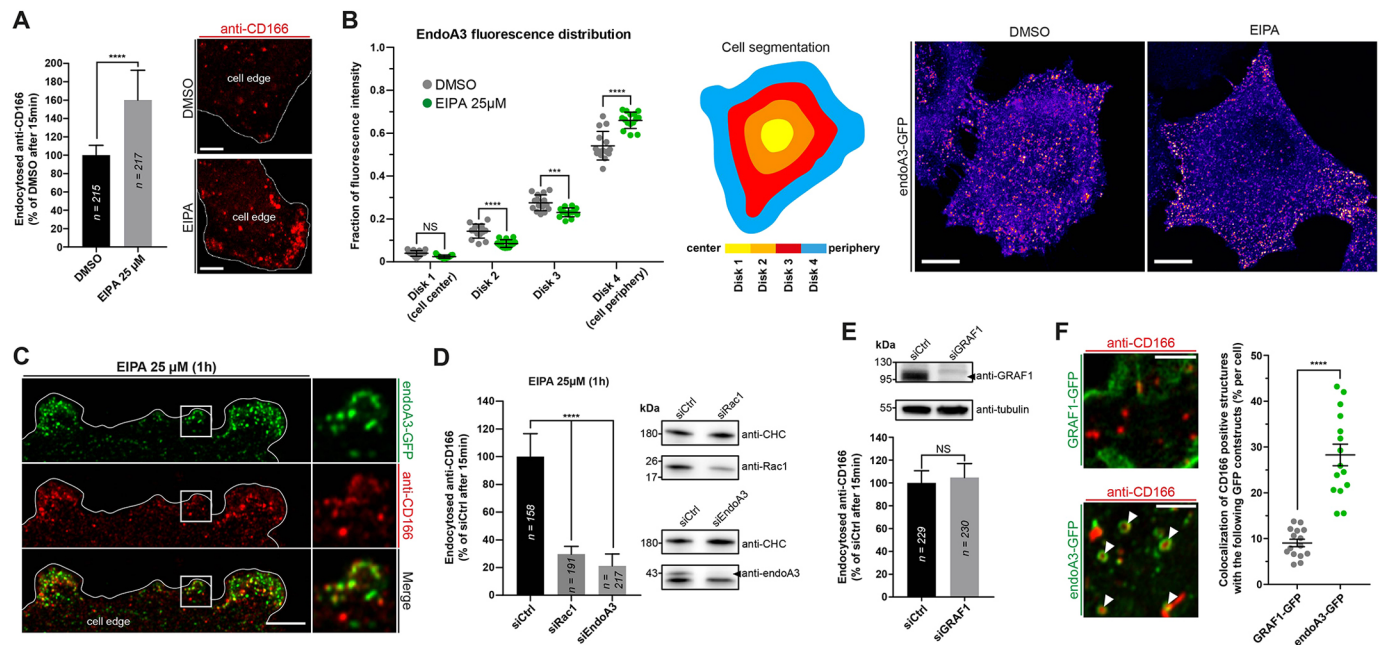


Fig. 4. EndoA3 mediated-endocytosis is distinct from macropinocytosis, FEME and CLIC/GEEC endocytosis. (A,D,E) Continuous uptake of anti-CD166 antibody for 15 min in HeLa cells. The remaining CD166 signal at the cell surface was stripped by acid washes on ice. Internal fluorescence was quantified from confocal images and plotted as the relative percentage of the control condition: DMSO for A, and negative control siRNA (siCtrl) for D and E. n cells, three independent experiments. **** $P < 0.0001$ (A and E, two-tailed unpaired Mann–Whitney t -test; D, two-sided Kruskal–Wallis test with Dunn’s multiple comparison post hoc test). Error bars are median with 95% c.i. (A) CD166 uptake in cells pre-incubated for 1 h with DMSO or 25 μ M EIPA. Images highlight bursts of CD166 endocytic carriers (red) at the cell edge in the EIPA condition. Cell border is depicted in white. (B) Quantification of GFP-tagged endoA3 distribution in cells incubated for 1 h with DMSO versus 25 μ M EIPA (left panel). 15 confocal images ($n=15$) were acquired for each condition (two or three cells per image, representative images in the right panel). Cells were segmented into four disks (see central panel) to measure fluorescence distribution with Cell profiler software. Three independent experiments. NS, not significant; *** $P < 0.001$, **** $P < 0.0001$ (two-way ANOVA with Sidak’s multiple comparison test). Error bars are mean \pm s.e.m. Representative images of each treatment in the right panel. (C) Continuous anti-CD166 uptake in HeLa cells stably expressing GFP-tagged endoA3 and incubated for 1 h with 25 μ M EIPA. Cell border is depicted in white. (D) CD166 uptake in cells transfected with siRNAs against endogenous Rac1 or endoA3, and treated for 1 h with 25 μ M EIPA. (E) CD166 uptake in cells transfected with siRNAs against endogenous GRAF1. (F) Continuous anti-CD166 uptake (red) in HeLa cells transfected with GFP-tagged GRAF1 or endoA3 (green). Note the absence of overlap between GRAF1 and CD166 signals. White arrowheads indicate colocalization events. Quantifications of colocalization are shown on the graph. $n=15$ cells, three independent experiments. **** $P < 0.0001$ (two-tailed unpaired Mann–Whitney t -test). Error bars are mean \pm s.e.m. Western blots in panels D and E highlight knockdown efficiency. Scale bars: 5 μ m (A,C), 10 μ m (B), 2 μ m (F).

of CD166 endocytosis – 70% inhibition upon Rac1 depletion and 79% inhibition upon endoA3 depletion (Fig. 4D; representative images in Fig. S4E). These observations are in sharp contrast with what is seen in untreated cells, where Rac1 or endoA3 depletions induce a milder reduction of CD166 uptake, in a range of 40–50% (see Fig. 3C and our previous publication; Renard et al., 2020). These results suggest that a fraction of CD166 can be retrieved from the plasma membrane via macropinocytosis, in addition to the specific endoA3-mediated CIE mechanism. More interestingly, these data highlight the existence of compensatory regulation mechanisms between endoA3-mediated CIE and macropinocytosis.

Finally, we investigated the effect of GRAF1 (also known as ARHGAP26) depletion on CD166 uptake. GRAF1 is a BAR domain protein known to function in CLIC/GEEC endocytosis (Lundmark et al., 2008), which requires Cdc42 activation (Rossatti et al., 2019). Notably, endoA3-mediated CIE of CD166 shares strong similarities with CLIC/GEEC endocytosis, as both endocytic modalities operate according to the GL-Lect hypothesis, in which clustering of glycosphingolipids and glycosylated proteins at the cell surface is driven by galectins and is required to drive the formation of endocytic invaginations (Lakshminarayan et al., 2014; Renard et al., 2020). The depletion of GRAF1 did not show any effect on CD166 endocytosis (Fig. 4E; representative images in Fig. S4F). Accordingly, low colocalization levels between GFP-tagged GRAF1 and CD166-positive puncta was observed, in

contrast to endoA3-GFP (Fig. 4F). To conclude, in combination with our previously published data (Renard et al., 2020), these new observations further indicate that endoA3-mediated endocytosis of CD166 is a process distinct from macropinocytosis, FEME and CLIC/GEEC mechanisms.

Microtubules and kinesin motors play a central role in the endocytosis of CD166

To examine whether microtubules in the lamellar region are important for CD166 uptake, we treated cells with nocodazole – a strong inhibitor of microtubule polymerization (Lee et al., 1980) – and then assessed their ability to internalize CD166. We also looked at the uptake of established CIE cargoes, such as CD98 (a heterodimer of SLC3A2 and SLC7A5) or MHCI, and the canonical CME cargo transferrin. Remarkably, nocodazole treatment drastically decreased CD166 uptake (–75%), whereas transferrin, CD98 and MHCI uptake were not or only slightly affected (Fig. 5A). Instead, treatment with nocodazole mostly resulted in scattered transferrin-, CD98- and MHCI-positive endosomes at the cell periphery (Fig. 5A; Fig. S5A). Of note, the surface levels of these proteins were slightly reduced in the presence of nocodazole (–7% for CD166 to –16% for MHCI, Fig. S5B), most likely due to sorting defects, as documented by Maldonado-Baez et al. (2013). To our knowledge, CD166 is the first transmembrane cargo, other than bacterial toxins (Day et al.,

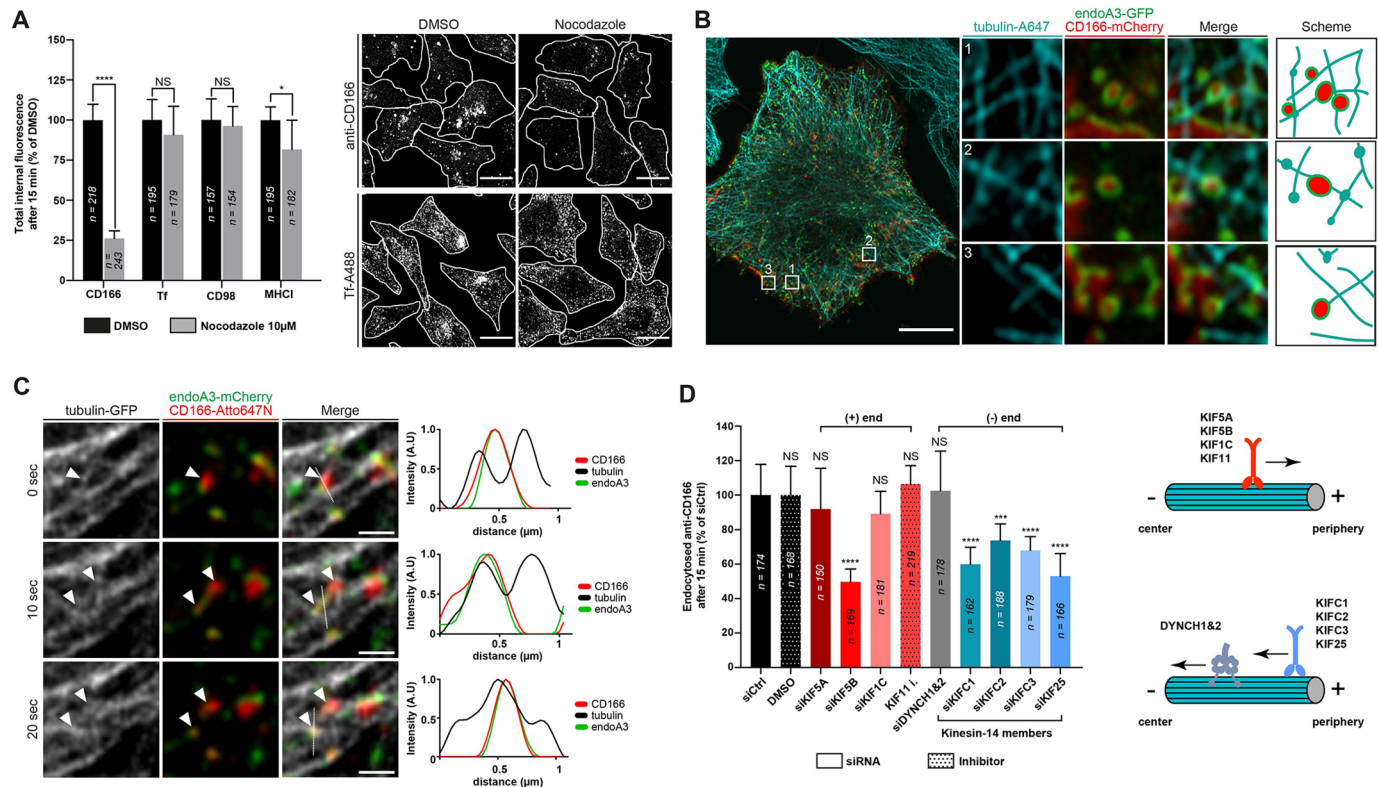


Fig. 5. Microtubules and kinesin motors drive the endoA3-mediated CIE of CD166. (A,D) Continuous uptake of antibodies (anti-CD166, anti-CD98 or anti-MHC1) or Alexa Fluor 488-labeled transferrin (Tf) for 15 min in HeLa cells. The remaining signal at the cell surface was stripped by acid washes on ice. Internal fluorescence was quantified from confocal images and plotted as the relative percentage of the control condition: DMSO in A and D, negative control siRNA (siCtrl) in D. *n* cells, three independent experiments. NS, not significant. **P*<0.05, ****P*<0.001, *****P*<0.0001 (A, two-tailed unpaired Mann–Whitney *t*-test; D, two-sided Kruskal–Wallis test with Dunn’s multiple comparison post hoc test). Error bars are median with 95% c.i. (A) CD166, Tf, CD98 and MHC1 uptake in cells pre-incubated for 1 h with DMSO or 10 μM nocodazole. Representative images of anti-CD166 and Tf-A488 condition in the right panel. Cell border is depicted in white. (B) Continuous anti-CD166 uptake and α -tubulin labeling in HeLa cells stably expressing GFP-tagged endophilin-A3. Image representative of three independent experiments. (C) Live acquisitions of HeLa cells co-transfected with mCherry-tagged endoA3 and GFP-tagged tubulin and incubated with Atto647N-labeled anti-CD166 primary antibody. Note the tubulation (10 s) and scission (20 s) of an endoA3-positive CD166 carrier, as indicated by the white arrowheads. Intensity profile plots highlight the superposition of fluorescent signals. The dashed line indicates intensity profile origins. Images are extracted from time series of 30 frames, with a 10 s interval between each frame. Three independent experiments. (D) CD166 uptake (left panel) in cells transfected with siRNAs against endogenous dynein heavy chains 1 and 2 (DYNCH1&2), KIF5A, KIF5B, KIF1C, KIFC1, KIFC2, KIFC3 and KIF25 or treated for 1 h with DMSO or 200 μM monastrol (KIF11 inhibitor). Scheme depicts dynein or kinesin motor directions along microtubules (right panel). Scale bars: 20 μm (A), 10 μm (B), 1 μm (C).

2015) or macropinocytic cargoes (Williamson and Donaldson, 2019), to heavily rely on microtubules for its endocytosis.

Accordingly, immunofluorescence experiments revealed CD166 carriers in close association with the microtubule network (Fig. 5B). This association was monitored dynamically by confocal live-cell imaging, with endoA3-positive CD166 carriers moving along microtubules (Fig. S5C, Movie 7). Interestingly, some tubulation and scission events of endoA3-positive CD166 structures along microtubules could be observed (Fig. 5C). Previous spinning-disk live-cell experiments highlighted similar CD166 and endoA3-positive tubular invaginations emanating from the cell surface, which displayed fission events that might occur through FDS (Renard et al., 2020). Consequently, we questioned whether microtubule-based motors could potentiate endocytic carrier formation or scission during CD166 endocytosis, as previously reported for bacterial toxins (Renard et al., 2015). To do so, we measured CD166 uptake in cells treated with siRNAs and inhibitors targeting dynein and kinesin motors (Fig. 5D; representative images in Fig. S6A). Surprisingly, depletion of dynein 1 and 2 heavy chains (western blot in Fig. S6B) had no effect on CD166 uptake, which is in stark contrast with the FDS of bacterial toxin-containing and FEME carriers (Renard et al., 2015; Simunovic et al., 2017; Ferreira et al., 2021). On the other hand,

the silencing of each individual member of the minus-end kinesin-14 subfamily significantly reduced CD166 uptake, especially in the case of KIFC1 (–41%) and KIF25 (–47%) depletion. Notably, the sum of their respective effects on CD166 uptake exceeds 100%, which could reflect a cooperative function of these motors in the process. In that direction, the combined depletion of all kinesin-14 members showed a decrease of CD166 uptake (–49%, Fig. S6C) to a similar extent to that seen upon the depletion of KIF25 alone. As observed for dyneins, depletion of most plus-end kinesins tested in our study had no effect on CD166 endocytosis, except for KIF5B (a kinesin-1 heavy chain) whose depletion resulted in a noticeable decrease of uptake (–50%, western blot in Fig. S6B). This is surprising, since KIF5B is generally involved in plus-end motor activity, such as vesicle transport to the cell periphery (Endow et al., 2010). Here, opposing forces resulting from both plus- and minus-end kinesin motors might be required for vesicle fission, as proposed by Nath et al. (2007) for KIF5B and KIFC1. In line with this hypothesis, depletion of KIF5B together with KIFC1 or KIF25 further accentuated, although not significantly, the inhibition of CD166 uptake (–60%, Fig. S6C). While these observations would require further investigation, they point to a potential role of minus-end kinesin members and KIF5B in this endocytic modality.

DISCUSSION

In the present study, we carried out a functional and visual molecular screen with the aim to identify new molecular players involved in endoA3-dependent CIE. First, we demonstrate that the actin cytoskeleton is dynamically associated with CD166 endocytic carriers and that its disruption strongly inhibits the endoA3-dependent uptake of CD166. In addition, the actin-dependent molecular motor myosin 2A contributes to the mechanism, as recently shown for the CIE of MHC1 (Wayt et al., 2021). Myosin 2A probably regulates actin contractility and membrane tension near CD166 uptake sites.

Next, we showed that the Rho GTPase Rac1, but not Cdc42, is required to mediate CD166 endocytosis. This function of Rac1 is partially controlled by the GEF Tiam1, which was previously shown to interact with endoA3 in a process modulating cancer cell migration (Minard et al., 2006). These results are in stark contrast with FEME, in which both Rac1 and especially Cdc42 act as master regulators of the process. Of note, results obtained upon EIPA treatment (Fig. 4) suggest that a fraction of CD166 can be internalized from plasma membrane via macropinocytosis, in addition to the specific endoA3-mediated CIE mechanism that we identified. In particular, these data point out the existence of compensatory regulations between endoA3-mediated CIE and macropinocytosis. Although it remains unknown how this regulation is orchestrated at the molecular level, a tempting hypothesis is that inhibition of macropinocytosis with EIPA increases the availability of Rac1 for endoA3-dependent CIE of CD166. On the other hand, while both CLIC/GEEC and endoA3-dependent endocytosis operate according to the GL-Lect hypothesis, these endocytic modalities show differences in the type of BAR domain proteins (GRAF1 and IRSp53 versus endoA3) and regulatory Rho GTPases (Cdc42 versus Rac1) they require (Lundmark et al., 2008; Rossatti et al., 2019; Sathe et al., 2018). Notably, we have recently shown that galectin-3 – previously shown to be involved in the biogenesis of some CLIC populations (Lakshminarayanan et al.,

2014) – does not seem to drive the endoA3-mediated CIE of CD166 (Renard et al., 2020), which further strengthens the idea that the current endoA3-mediated mechanism is distinct from the canonical CLIC/GEEC route.

Rac1 is a well-known upstream activator of myosin 2 activity. This Rho GTPase activates Rho-associated coiled-coil kinases (ROCKs), which in turn inhibit myosin light chain phosphatase (MLCP), resulting in the activation of myosin 2-based actin contractility (Amin et al., 2013). The activation of the ROCK1 isoform by Rac1 has been shown to prevent PI(4,5)P2-dependent tubule formation, presumably by enhancing tubule scission through local membrane tension increase (Soriano-Castell et al., 2017). Similarly, Wyat et al. (2021) demonstrated that ROCK2 isoform controls the CIE of MHC1 and CD59 via promotion of myosin 2 activity. Therefore, in the case of CD166 uptake, endoA3 might activate the Rac1/ROCK axis via the recruitment of Tiam1, leading to actin remodeling and local membrane tension increase through myosin 2A activation (Fig. 6). In parallel, our data also support a direct role of well-established Rac1 effectors, such as WAVE and the ARP2/3 complex (Chen et al., 2017) in the polymerization actin in endoA3-mediated CIE (Fig. 6). In a more physiological context, numerous studies have reported elevated Rac1 signaling events (Espina et al., 2008; Gomez del Pulgar et al., 2005; Kotelevets and Chastre, 2020) as well as high Tiam1 expression in colorectal cancer (Minard et al., 2006, 2005), in which CD166 is strongly dysregulated (Hansen et al., 2013; Lugli et al., 2010; Ribeiro et al., 2016; Zhang et al., 2017). Here, in addition, we propose that the endoA3/TIAM1/Rac1 axis activates an endocytic mechanism that enables cancer cells to downregulate the cell surface levels of certain proteins, such as CD166, which would allow them to tune their migratory and adhesive properties. Further investigations will be necessary to validate this model.

Finally, we present pieces of evidence that microtubules and molecular motors provide an important source of mechanical forces

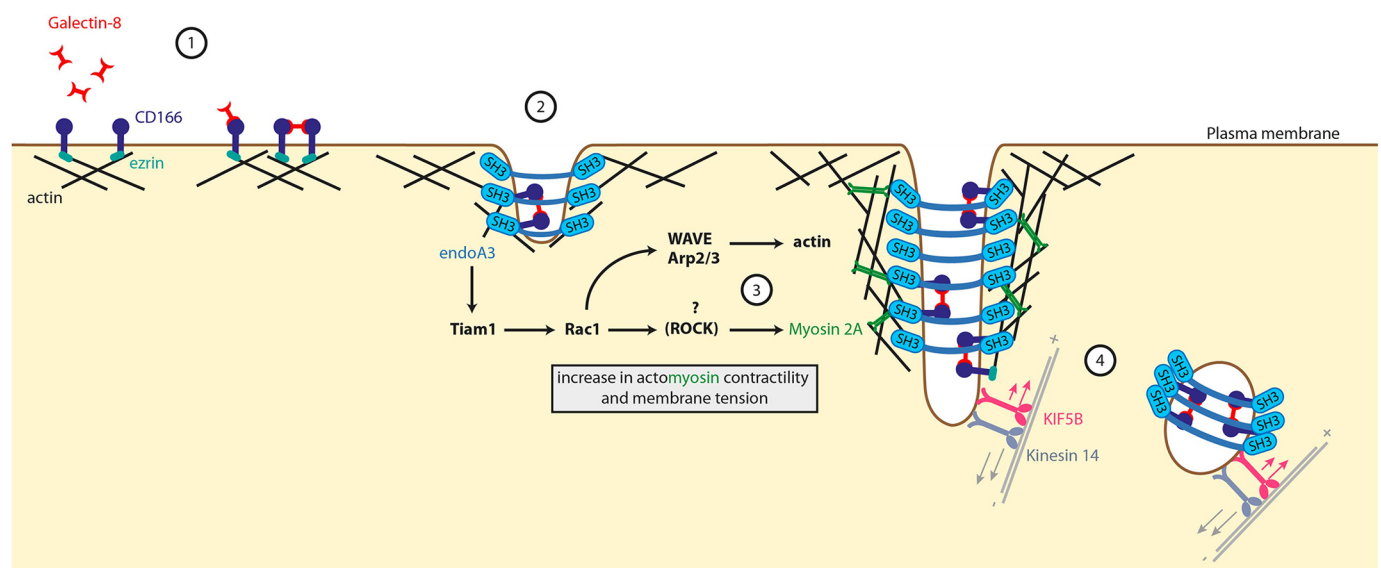


Fig. 6. Working model for endoA3-mediated endocytosis of CD166. CD166 carrier formation initiates with the clustering of CD166 molecules driven by extracellular galectin-8 at the cell surface (1), which is followed by the recruitment of endoA3 that further increases plasma membrane curvature (2). EndoA3 recruitment at CD166 uptake sites stimulates carrier formation via Tiam1 binding, which in turn activates the Rac1/ROCK axis leading to actin remodeling and increased membrane tension through myosin 2A activity (3). Rac1 can also directly modulate branched actin nucleators (WAVE, ARP2/3 complex). Stimulation of actin polymerization and contraction of actin filaments by myosin 2A locally increases membrane tension, which facilitates membrane fission – possibly through FDS – with nascent endocytic carriers pulled along microtubule by kinesin motors (KIF5B and kinesin-14?) and endoA3 providing the BAR domain scaffold that generates friction (4).

that drive either the formation or the scission of CD166 endocytic carriers. Such possibility has been previously described for bacterial toxin endocytosis, where an FDS mechanism (involving scaffolding of a membrane tube by the BAR domain protein endoA2 and pulling forces provided by dynein) acts in synergy with actin and dynamin to potentiate endocytic carrier release from the plasma membrane (Renard et al., 2015; Simunovic et al., 2017). Here, minus-end kinesin-14 members – but not dynein – seem to be the main microtubule-based motors involved. These motors presumably act in cooperation, as their combined depletion does not further reduce CD166 uptake. Surprisingly, depletion of the plus-end kinesin KIF5B also resulted in a strong decrease of CD166 uptake. Opposing forces resulting from both plus- and minus-end kinesin motors might facilitate vesicle scission, potentially by increasing longitudinal tension along endocytic carriers. Although the physiological reasons for opposing motors acting on the same cargo are not clear, such a molecular display is not rare and has been reported for many intracellular structures (Stephens, 2012). Nevertheless, we cannot exclude an indirect effect of KIF5B depletion on CD166 uptake due to its important role in anterograde transport (Serra-Marques et al., 2020) and organelle positioning (Gupta et al., 2008). The myosin 2A actin motor might also contribute to membrane tubulation in conjunction with kinesin motors. Such cooperation between actin- and microtubule-based motors has been demonstrated *in vitro* for myosin 1C and KIF5A (McIntosh et al., 2018) or *in vivo* for myosin 2A and KIF5B (Miserey-Lenkei et al., 2010). A possible mechanism is that contraction of actin filaments by myosin 2A locally increases membrane tension, which will in turn facilitate membrane fission through FDS, with nascent endocytic carriers pulled along microtubule by kinesin motors, and with endoA3 providing the scaffold that generates friction (Fig. 6). Still, additional investigations will be required to see whether CD166 carriers undergo FDS. In addition, live-cell imaging and super resolution microscopy approaches with kinesin candidates should be considered to confirm their association with CD166–endoA3-positive carriers.

Collectively, our data reveals new molecular players involved in the endoA3-dependent CIE modality and further distinguishes the mechanism from other unconventional endocytic processes such as macropinocytosis, FEME or CLIC/GEEC endocytosis. Our study also highlights potential compensation phenomena between endoA3-dependent CIE and macropinocytosis. To date, crosstalk, competition and potential compensatory regulations between endocytic mechanisms remain poorly explored. This situation calls for future studies on these important aspects, which will constitute important milestones in the field.

MATERIALS AND METHODS

Antibodies and other reagents

The following antibodies were purchased from the indicated suppliers: mouse monoclonal anti-CD166 clone 3A6 (Bio-Rad, MCA1926, 1:250 for immunofluorescence and flow cytometry); rabbit monoclonal anti-endoA1 (Cell Signaling Technology, 65469, 1:1000 for western blotting); mouse monoclonal anti-endoA2 (Santa Cruz Biotechnology, sc-365704, 1:500 for western blotting); rabbit polyclonal anti-endoA3 (Sigma Life Sciences, HPA039381, 1:1000 for western blotting); mouse monoclonal anti-clathrin heavy chain (BD Biosciences, 610500, 1:5000 for western blotting); mouse monoclonal anti- α -tubulin (Sigma, T5168, 1:5000 for western blotting); rabbit polyclonal anti-myosin IIA (Sigma, M8064, 1:2000 for western blotting, 1:200 for immunofluorescence); rabbit polyclonal anti-myosin IIB (Biolegend, 909902, 1:2000 for western blotting, 1:200 for immunofluorescence); mouse monoclonal anti-CD98 (Biolegend, clone MEM-108, 315602, 1:250 for immunofluorescence);

mouse monoclonal anti-MHCI (Biolegend, clone W6/32, 311402, 1:250 for immunofluorescence); rabbit polyclonal anti-Tiam1 (Bethyl, A300-0994A-T, 1:1000 for western blotting); mouse monoclonal anti-Rac1 (Merck Millipore, 05-389-25UG, 1:1000 for western blotting); rabbit polyclonal anti-GRAF1 (Bethyl, A304-340A-T, 1:1000 for western blotting); mouse monoclonal anti-Cdc42 (Cytoskeleton Inc., ACD03-S, 1:250 for western blotting); rabbit polyclonal anti-DYNC1H1 (Proteintech, 123456-1-AP, 1:1000 for western blotting); rabbit polyclonal anti-KIF5B (Bethyl, A304-306A-T, 1:1000 for western blotting); rabbit polyclonal anti-ARPC2 (Bethyl, A305-394A-T, 1:1000 for western blotting), secondary antibodies conjugated to Alexa Fluor 488, 546, or 647 (Thermo Fisher Scientific, 1:250 for immunofluorescence); and anti-mouse-IgG and anti-rabbit-IgG secondary antibodies conjugated to horseradish peroxidase (Sigma and Dako, respectively). Phalloidin–Alexa Fluor 555 was purchased from Cell Signaling Technology (8953S, 1:5000 for immunofluorescence). Latrunculin A (L5163), Nocodazole (M1404), CK636 (C7374), ML141 (SML0407) and Monastrol (M8515) were purchased from Sigma. EIPA (3378) and Cytochalasin D (1233) were purchased from Tocris, Jasplakinolide (SC-202191) from Santa Cruz Biotechnology, NSC668394 (341216) from Calbiochem and human transferrin–Alexa Fluor 488 conjugate (T13342, 1:500 for immunofluorescence) from Thermo Fisher Scientific.

Cell culture

HeLa (human cervix adenocarcinoma, ATCC® CCL-2) were grown at 37°C under 5% CO₂ in Dulbecco's modified Eagle's medium (DMEM) high-glucose glutamax (Gibco, 61965-059) supplemented with 10% FBS, 100 U ml⁻¹ penicillin, 100 μ g ml⁻¹ streptomycin and 1 mM pyruvate. HeLa cells stably expressing endoA3–GFP (Renard et al., 2020) were grown in the same medium as the mother cell line, supplemented with 0.125 mg ml⁻¹ G418 (Roche, 04727878001).

DNA constructs and transfection

Expression plasmids for N-terminally GFP-tagged Rac1 WT, N17 and V12, and Cdc42 N17 (Florence Niedergang, Cochin Institute, Paris, France), N-terminally GFP-tagged Cdc42 WT (Anne Ridley, King's College London, UK), mCherry-tagged μ 2 subunit of AP2 complex (Christien Merrifield, Paris-Saclay University, France), and GFP-tagged GRAF1 (Richard Lundmark, Umea University, Sweden), were kindly provided by the indicated colleagues. N-terminally GFP-tagged Cdc42 L61 (12600), GFP-tagged α -tubulin (#12298), mCherry-WASF2 (#55161), and C-terminally tagged ARPC2-mCherry (#54979) were purchased from Addgene. The C-terminally GFP-FKBP-tagged human endoA3 construct was previously engineered in our laboratory (see Renard et al., 2020). For immunofluorescence and live-cell imaging experiments, plasmids were transfected with FuGene HD (Promega) in HeLa cells according to the manufacturer's instructions. Cells were used for experiments 16–24 h after transfection.

RNA interference

siRNAs used in this study were purchased from Qiagen and transfected with HiPerFect (Qiagen) according to the manufacturer's instructions to reach efficient knockdown. Experiments were always performed 72 h after siRNA transfection, where protein depletion efficiency was maximal as shown by immunoblotting analysis with specific antibodies (routinely 80–100%). For most experiments, cells were replated 24 h before use, according to the needs of the experiment. AllStars Negative Control siRNA (siCtrl) served as a reference point. Depletion of endoA isoforms, Rac1, Tiam1 and GRAF1 were achieved with two different sequences, at a total final concentration of 40 nM: endoA1 #1 (SI04149411: 5'-AAAGACTCTTTGGACATAGAA-3'), endoA1 #2 (SI04260949: 5'-AAATCTGGTATCCAAGCTTAA-3'), endoA2 #1 (SI03057250: 5'-CACCAGCAAGGCGGTGACAGA-3'), endoA2 #2 (SI03073931: 5'-CATGCTCAACACGGGTGTCCAA-3'), endoA3 #1 (SI04170376: 5'-CCAGACGAGAATACAAGCCAA-3') and endoA3 #2 (SI04176529: 5'-CCAGACGAAGAAGTCAGACAA-3'), Rac1 #1 (SI03065531: 5'-CAGACGTGTCCCGACATAA-3') and Rac1 #2 (SI03040884: 5'-ACGAAGTGGAGATTTACACTA-3'), Tiam1 #1 (SI00049819: 5'-ACGGCGAGCTTTAAGAAGAAA-3') and Tiam1

#2 (SI03066259: 5'-CAGCCCCAGGAAGACATCTAT-3'), GRAF1 #1 (SI02641247: 5'-AGGGAGTATACTAGTAGGTTA-3') and GRAF1 #2 (SI03077690: 5'-CCCCATATGCCTCTACCAAT-3'). For Cdc42 depletion, a single siRNA sequence at a final concentration of 40 nM was used (SI04381671: 5'-GGCGATGGTGTCTGTTGGTAA-3'). For myosin 2A and 2B depletion, we ordered custom siRNA sequences against each protein (5'-GGCCAAAGAGAACGAGAAGUU-3' and 5'-AAGGAUCGCUACUAUUCAGGA-3', respectively), that were previously validated by Wayt et al. (2021). All kinesins were knocked down using one siRNA sequence at a final concentration of 40 nM: KIF5A (SI00070994: 5'-AAGGGTTGTACTGAACGCTTT-3'), KIF5B (SI02781317: 5'-AACGTTGC-AAGCAGTTAGAAA-3'), KIF1C (SI02781331: 5'-CTGGAGAATCAG-TACCGGAAA-3'), KIFC1 (SI02653336: 5'-TCGGGAAACACAGGC-CATTA-3'), KIFC2 (SI03019884: 5'-CCAGATGGATCCACATCC-CAA-3'), KIFC3 (SI03035676: 5'-AAGGCTGTGCACGAGAATCTA-3'), and KIFC25 (SI03075506: 5'-CCAGGTCTCACCTGATAATTA-3'). Depletion of dynein heavy chain 1 and 2 were achieved using a mixture of eight siRNAs at a final concentration of 40 nM, as performed by Renard et al. (2015): DYNC2H1 #1 (SI04306841), DYNC2H1 #2 (SI04159134), DYNC2H1 #3 (SI04339559), DYNC2H1 #4 (SI04349184), DYNC1H1 #1 (SI02626141: 5'-CAGGTGGGTGTACATTACGAA-3'), DYNC1H1 #2 (SI02626162: 5'-AAGGAGGTTCTTAGCAAATTT-3'), DYNC1H1 #3 (SI02626148: 5'-CAGGAGGTAATTGCAGACAAA-3'), and DYNC1H1 #4 (SI02626155: 5'-CCCGTGATTGATGCAGATAAA-3'). Finally, depletion of ARPC2 was achieved using a mixture of 4 siRNAs, used at a final concentration of 40 nM, purchased from Dharmacon (SO-3017698G): ARPC2 #1 (J-012081-05: 5'-CCATGTATGTTGAGTCTAA-3'), ARPC2 #2 (J-012081-06: 5'-GCTCTAAGGCCTATATTCA-3'), ARPC2 #3 (J-012081-07: 5'-GGACAGAGTCACAGTAGTC-3'), ARPC2 #4 (J-012081-08: 5'-GTACGGGAGTTTCTTCCTA-3').

Confocal microscopy

For immunofluorescence studies, cells were fixed with 4% paraformaldehyde at 37°C for 20 min or on ice for 10 min followed by an additional 10 min at room temperature, depending on the requirements of each experiment. After quenching with 50 mM NH₄Cl for 10 min and permeabilization with saponin [0.02% saponin and 0.2% bovine serum albumin (BSA) in phosphate-buffered saline (PBS)] for 30 min, both at room temperature, cells were incubated with primary and/or secondary antibodies for 40 min, and mounted with Fluoromount G (Invitrogen). Fixed samples were imaged with a 34-channel Zeiss LSM 710 confocal microscope equipped with Airyscan system and with a Plan Apo 63× numerical aperture (NA) 1.4 oil immersion objective.

Live-cell confocal microscopy

HeLa cells stably expressing endoA3-GFP or HeLa cells were transfected with specified plasmids 16 to 24 h before the day of the experiment and grown on chambered glass coverslips (μ-slides with glass bottom, Ibidi) to reach subconfluence the next day. Time series of 30 or 60 frames, with a 10 s interval between each frame, were acquired with a 34-channel Zeiss LSM 710 confocal microscope equipped with Airyscan system and with a Plan Apo 63× numerical aperture (NA) 1.4 oil immersion objective. Observations were made at 37°C and 5% CO₂. If required, Atto647-labeled anti-CD166 antibody was added in the medium (5 μg ml⁻¹). Montages, kymographs, and movies were prepared with Fiji software (NIH).

Live-cell TIRF microscopy

HeLa cells transiently expressing the indicated plasmids were grown on chambered glass coverslips (μ-slides with glass bottom, Ibidi) to reach subconfluence the next day. Two-color time series of 61 or 121 frames, with a 2 s interval between each frame, were acquired with a Zeiss Axio Observer inverted microscope equipped with Plan Apo TIRF 100× NA 1.46 oil immersion objective, an iLas2 azimuthal TIRF module (Gataca Systems) and a stage top incubator (Tokai Hit). Observations were made at 37°C and 5% CO₂. Montages, kymographs and movies were prepared with Fiji software (NIH).

Uptake assays

HeLa cells or cells transfected with specified siRNAs or plasmid constructs were seeded in four-well plates 16–24 h before the experiment, in order to reach subconfluence the following day. On the day of the experiment, cells were first pre-incubated for 30 min at 37°C in fresh serum-containing medium (+25 mM Hepes) for CD166 uptake, and serum-free medium (+25 mM Hepes) for transferrin uptake. For uptake assays using molecular inhibitors, indicated inhibitor concentrations were systematically added in the medium and the pre-incubation period was extended from 30 min to 1 h depending on the inhibitor, as specified. Following pre-incubation, endocytosis was triggered by incubating cells at 37°C in the continuous presence of anti-CD166 antibody (5 μg ml⁻¹) or fluorescently labeled transferrin (Tf-A488, 10 μg ml⁻¹) in pre-warmed culture medium for 15 min. Endocytosis was stopped on ice, and unbound ligands were removed by extensive washes with ice-cold PBS supplemented with 1 mM Ca²⁺ and 0.5 mM Mg²⁺ (PBS++). Residual cell surface-accessible anti-CD166 antibody or Tf-A488 was stripped by three 20-s acid washes on ice (200 mM acetic acid, pH 2.5, 300 mM NaCl, 5 mM NaCl, 1 mM CaCl₂, and 1 mM MgCl₂). After neutralization by extensive washes with ice-cold PBS++, cells were fixed, permeabilized, incubated with secondary antibodies if necessary, and mounted as previously described (see the 'Confocal microscopy' section). Samples were imaged, and internalized fluorescent signals were quantified as explained below.

Flow cytometry

For uptake assays, endocytic levels quantified by confocal microscopy were corrected by their respective steady-state CD166 or Tf cell surface levels using flow cytometry. Briefly, cells were put on ice and washed three times with ice-cold PBS++. Next, cells were incubated for 10 min with PBS++ supplemented with 0.2% BSA (Sigma), followed by a second incubation with the same buffer containing anti-CD166 primary antibody (5 μg ml⁻¹) or fluorescently labeled transferrin (Tf-A488, 10 μg ml⁻¹) for 30 min. Afterwards, cells were washed three times with PBS++ with 0.2% BSA and then incubated for 30 min with a secondary Alexa-labeled antibody, if required. Finally, cells were washed three times with PBS and incubated for 45 min with a solution containing 4 mM EDTA in PBS to resuspend cells for flow cytometry analysis. Note that every incubation step was performed on ice with ice-cold (4°C) solutions to prevent endocytosis. Measurements were made with a Guava easyCyte (Merck-Millipore) flow cytometer (10,000 cells were counted per condition).

Colocalization assays

Cells transfected with indicated plasmid constructs were seeded in four-well plates, 16–24 h before the experiment, in order to reach subconfluence the following day. The day of the experiment, cells were pre-incubated for 30 min at 37°C in fresh serum-containing medium (+25 mM Hepes) for CD166 uptake. For experiments using molecular inhibitors, the pre-incubation period was extended to 1 h and performed with indicated inhibitor concentrations. Endocytosis was then triggered by incubating cells at 37°C in the continuous presence of anti-CD166 antibody (5 μg ml⁻¹) in pre-warmed culture medium for 15 min (with or without inhibitor). Cells were then washed with pre-warmed PBS to remove unbound antibodies. Afterwards, cells were fixed with 4% paraformaldehyde at 37°C for 20 min, permeabilized, incubated with secondary antibodies, and mounted as previously described (see the 'Confocal microscopy' section). Samples were imaged, and colocalization levels were quantified as detailed below.

Quantification of cargo uptake from confocal images

Confocal images were quantified using Icy v2.2 (Institut Pasteur) software. Briefly, regions of interest (ROIs) were drawn manually around each cell. Within each cellular ROI, bright spots corresponding to endocytic structures were automatically detected over dark background using the 'Spot Detector' plugin. The plugin performs image denoising by computing wavelet adaptive thresholding (WAT) on the union of all ROIs present in an image. This automatic thresholding was then manually adjusted, depending on the size of the spots – for each independent experiment, we chose scale 2 and adjusted sensitivity empirically. In addition, we added a size filter to discard

small spots up to 4 pixels. As an output, we obtained the number of endocytic structures within each cell and their respective intensities, which we summed to obtain the total uptake of the cargo per cell. For each experiment, data were normalized to the control condition (set as 100%). Of note, endocytic levels were corrected to the respective cell surface levels measured by flow cytometry, relatively to the control condition (set as 100%).

Quantification of colocalization

Quantification of colocalization between two channels was performed using ImageJ/Fiji v2.0.0-rc-65/1.51u (NIH) software. Briefly, an object-based method was used, as implemented in JACoP (Bolte and Cordelières, 2006), based on the coincidence between two centroids with a 2-pixel tolerance. This was achieved in ImageJ by first segmenting the tagged proteins by spot detection in each channel, finding their position, and growing them by dilation to a 2-pixel radius. The spot detection consisted of finding maxima in the images using the 'find maxima' plugin of ImageJ, whose noise tolerance parameter was set up visually independently for each channel. The results were expressed as the percentage of colocalizing spots over the total number of spots in one of the two channels. Regarding quantification of triple colocalization, a similar strategy combining detection of maxima and the JACoP plugin was used. First, centers of colocalizing spot between two channels (e.g. red and green) were isolated by overlapping dilated maxima of each channel, then using a color threshold to isolate overlapping regions (e.g. yellow), and finally by using the 'find maxima' plugin of ImageJ. Afterwards, isolated colocalizing centers were dilated to a 2-pixel radius and colocalization with the spots of the third channel (e.g. blue) was assessed using JACoP object-based colocalization method.

Quantification of fluorescence distribution

First, we extracted endoA3 spots from confocal images using Icy v2.2 software. Bright endoA3 spots were automatically detected over dark background using the 'Spot Detector' plugin. The threshold was manually adjusted, depending on the size of the spots – for each independent experiment, we chose scale 2 and adjusted sensitivity empirically. Next, we extracted the binary image resulting from the detection and used it to measure endoA3 distribution with Cell profiler software 4.1.3 (Broad Institute). The first step consisted of manually identifying cells using the 'IdentifyObjectsManually' module, and the second step was to measure fluorescence distribution within each object/cell using the 'MeasureObjectIntensityDistribution' module, with a segmentation into four scaled disks (bins) (see Fig. 4B). In this way, we could extract the mean endoA3 fluorescence fraction within each disk/bin for all confocal images (two or three cells per image) and extract the cellular distribution of endoA3 in different conditions.

Statistical analyses

All source data used to build the graphs in the main figures and supplementary figures are available in Tables S1–S9. All statistical analyses were performed using Prism v7 software (Graphpad Inc). The normality of datasets was checked with D'Agostino–Pearson omnibus normality test. In the case of Gaussian distributions, parametric tests were used, and data were represented on graphs as mean±s.e.m. as error bars. In the case of non-Gaussian distributions, nonparametric tests were used, and data were represented on graphs as median±95% c.i. as error bars. Details on the parametric and nonparametric tests used for each analysis, as well as other statistical details related to specific graphs, are indicated in figure legends. Significance of comparisons is represented on the graphs by asterisks. No statistical method was used to predetermine sample size.

Acknowledgements

We would like to acknowledge the following people for providing DNA constructs: F. Niedergang (Cochin Institute), A. Ridley (King's College London) and R. Lundmark (Umea University). We thank Alison Forrester (Institut Curie) for critical reading of the manuscript; B. Knoops, P. Dumont, and F. Gofflot from LIBST (UCLouvain) for sharing cell culture and flow cytometry facilities, and materials. Finally, we acknowledge the following imaging core facilities: IMABIOL (LIBST, UCLouvain), Morph-Im (UNamur).

Competing interests

The authors declare no competing or financial interests.

Author contributions

Conceptualization: F.T., H.-F.R.; Methodology: F.T., H.-F.R.; Validation: F.T., N.Z., H.-F.R.; Formal analysis: F.T.; Investigation: F.T., N.Z.; Resources: F.T., P.M., H.-F.R.; Data curation: F.T.; Writing - original draft: F.T.; Writing - review & editing: F.T., P.M., H.-F.R.; Visualization: F.T.; Supervision: P.M., H.-F.R.; Project administration: P.M., H.-F.R.; Funding acquisition: P.M., H.-F.R.

Funding

F.T. is supported by a FRIA (Fonds pour la Formation à la Recherche dans l'Industrie et l'Agriculture) PhD fellowship from Fonds de la Recherche Scientifique (FNRS; Belgium). P.M. is supported by grants from the Fonds de la Recherche Scientifique (FNRS, CDR-J.0119.19) and the 'Communauté française de Belgique–Actions de Recherches Concertées' (17/22-085). H.-F.R. is supported by a Start-Up Grant Collen-Francqui from Francqui Foundation (Belgium) and an Incentive Grant for Scientific Research from the Fonds de la Recherche Scientifique (FNRS, MIS-F.4540.21).

Peer review history

The peer review history is available online at <https://journals.biologists.com/jcs/article-lookup/doi/10.1242/jcs.259623>.

References

- Amin, E., Dubey, B. N., Zhang, S. C., Gremer, L., Dvorsky, R., Moll, J. M., Taha, M. S., Nagel-Steger, L., Piekorz, R. P., Somlyo, A. V. et al. (2013). Rho-kinase: regulation, dysfunction, and inhibition. *Biol. Chem.* **394**, 1399–1410. doi:10.1515/hsz-2013-0181
- Bolte, S. and Cordelières, F. P. (2006). A guided tour into subcellular colocalization analysis in light microscopy. *J. Microsc.* **224**, 213–232. doi:10.1111/j.1365-2818.2006.01706.x
- Boucrot, E., Ferreira, A. P., Almeida-Souza, L., Debard, S., Vallis, Y., Howard, G., Bertot, L., Sauvonnet, N. and McMahon, H. T. (2015). Endophilin marks and controls a clathrin-independent endocytic pathway. *Nature* **517**, 460–465. doi:10.1038/nature14067
- Boulant, S., Kural, C., Zeeh, J. C., Ubelmann, F. and Kirchhausen, T. (2011). Actin dynamics counteract membrane tension during clathrin-mediated endocytosis. *Nat. Cell Biol.* **13**, 1124–1131. doi:10.1038/ncb2307
- Bubb, M. R., Spector, I., Beyer, B. B. and Fosen, K. M. (2000). Effects of jasplakinolide on the kinetics of actin polymerization. An explanation for certain *in vivo* observations. *J. Biol. Chem.* **275**, 5163–5170. doi:10.1074/jbc.275.7.5163
- Bulut, G., Hong, S. H., Chen, K., Beauchamp, E. M., Rahim, S., Kosturko, G. W., Glasgow, E., Dakshanamurthy, S., Lee, H. S., Daar, I. et al. (2012). Small molecule inhibitors of ezrin inhibit the invasive phenotype of osteosarcoma cells. *Oncogene* **31**, 269–281. doi:10.1038/ncr.2011.245
- Bye, C. R., Rytova, V., Alsanie, W. F., Parish, C. L. and Thompson, L. H. (2019). Axonal growth of midbrain dopamine neurons is modulated by the cell adhesion molecule ALCAM through trans-heterophilic interactions with L1cam, Chl1, and semaphorins. *J. Neurosci.* **39**, 6656–6667. doi:10.1523/JNEUROSCI.0278-19.2019
- Cayrol, R., Wosik, K., Berard, J. L., Dodelet-Devillers, A., Ifergan, I., Kebir, H., Haqqani, A. S., Kreymborg, K., Krug, S., Moudjian, R. et al. (2008). Activated leukocyte cell adhesion molecule promotes leukocyte trafficking into the central nervous system. *Nat. Immunol.* **9**, 137–145. doi:10.1038/ni1551
- Chan Wah Hak, L., Khan, S., Di Meglio, I., Law, A. L., Lucken-Ardjomande, Hasler, S., Quintaneiro, L. M., Ferreira, A. P. A., Krause, M., McMahon, H. T. and Boucrot, E. (2018). FBP17 and CIP4 recruit SHIP2 and lamellipodin to prime the plasma membrane for fast endophilin-mediated endocytosis. *Nat. Cell Biol.* **20**, 1023–1031. doi:10.1038/s41556-018-0146-8
- Chen, B., Chou, H. T., Brautigam, C. A., Xing, W., Yang, S., Henry, L., Doolittle, L. K., Walz, T. and Rosen, M. K. (2017). Rac1 GTPase activates the WAVE regulatory complex through two distinct binding sites. *Elife* **6**, e29795.
- Chitteti, B. R., Kobayashi, M., Cheng, Y., Zhang, H., Poteat, B. A., Broxmeyer, H. E., Pelus, L. M., Hanenberg, H., Zollman, A., Kamocka, M. M. et al. (2014). CD166 regulates human and murine hematopoietic stem cells and the hematopoietic niche. *Blood* **124**, 519–529. doi:10.1182/blood-2014-03-565721
- Coué, M., Brenner, S. L., Spector, I. and Korn, E. D. (1987). Inhibition of actin polymerization by latrunculin A. *FEBS Lett.* **213**, 316–318. doi:10.1016/0014-5793(87)81513-2
- Day, C. A., Baetz, N. W., Copeland, C. A., Kraft, L. J., Han, B., Tiwari, A., Drake, K. R., De Luca, H., Chinnappen, D. J., Davidson, M. W. et al. (2015). Microtubule motors power plasma membrane tubulation in clathrin-independent endocytosis. *Traffic* **16**, 572–590. doi:10.1111/tra.12269
- Egami, Y., Taguchi, T., Maekawa, M., Arai, H. and Araki, N. (2014). Small GTPases and phosphoinositides in the regulatory mechanisms of

- macropinosome formation and maturation. *Front Physiol* **5**, 374. doi:10.3389/fphys.2014.00374
- Endow, S. A., Kull, F. J. and Liu, H. (2010). Kinesins at a glance. *J. Cell Sci.* **123**, 3420–3424. doi:10.1242/jcs.064113
- Espina, C., Cespedes, M. V., Garcia-Cabezas, M. A., Gomez del Pulgar, M. T., Boluda, A., Oroz, L. G., Benitah, S. A., Cejas, P., Nistal, M., Mangues, R. et al. (2008). A critical role for Rac1 in tumor progression of human colorectal adenocarcinoma cells. *Am. J. Pathol.* **172**, 156–166. doi:10.2353/ajpath.2008.070561
- Ferragut, F., Vachetta, V. S., Troncoso, M. F., Rabinovich, G. A. and Elola, M. T. (2021). ALCAM/CD166: a pleiotropic mediator of cell adhesion, stemness and cancer progression. *Cytokine Growth Factor Rev.* **61**, 27–37. doi:10.1016/j.cytogfr.2021.07.001
- Ferreira, A. P. A., Casamento, A., Carrillo Roas, S., Halff, E. F., Panambalana, J., Subramaniam, S., Schutzenhofer, K., Chan Wah Hak, L., McGourty, K., Thalassinou, K. et al. (2021). Cdk5 and GSK3beta inhibit fast endophilin-mediated endocytosis. *Nat. Commun.* **12**, 2424. doi:10.1038/s41467-021-22603-4
- Fujimoto, L. M., Roth, R., Heuser, J. E. and Schmid, S. L. (2000). Actin assembly plays a variable, but not obligatory role in receptor-mediated endocytosis in mammalian cells. *Traffic* **1**, 161–171. doi:10.1034/j.1600-0854.2000.010208.x
- Gomez del Pulgar, T., Benitah, S. A., Valeron, P. F., Espina, C. and Lacal, J. C. (2005). Rho GTPase expression in tumorigenesis: evidence for a significant link. *BioEssays* **27**, 602–613. doi:10.1002/bies.20238
- Grassart, A., Dujancourt, A., Lazarow, P. B., Dautry-Varsat, A. and Sauvonnnet, N. (2008). Clathrin-independent endocytosis used by the IL-2 receptor is regulated by Rac1, Pak1 and Pak2. *EMBO Rep.* **9**, 356–362. doi:10.1038/embor.2008.28
- Graziano, B. R., Town, J. P., Sitarska, E., Nagy, T. L., Fosnaric, M., Penic, S., Iglic, A., Kralj-Iglic, V., Gov, N. S., Diz-Munoz, A. et al. (2019). Cell confinement reveals a branched-actin independent circuit for neutrophil polarity. *PLoS Biol.* **17**, e3000457. doi:10.1371/journal.pbio.3000457
- Gupta, V., Palmer, K. J., Spence, P., Hudson, A. and Stephens, D. J. (2008). Kinesin-1 (uKHC/KIF5B) is required for bidirectional motility of ER exit sites and efficient ER-to-Golgi transport. *Traffic* **9**, 1850–1866. doi:10.1111/j.1600-0854.2008.00811.x
- Hassan, N. J., Barclay, A. N. and Brown, M. H. (2004). Frontline: Optimal T cell activation requires the engagement of CD6 and CD166. *Eur. J. Immunol.* **34**, 930–940. doi:10.1002/eji.200424856
- Hansen, A. G., Freeman, T. J., Arnold, S. A., Starchenko, A., Jones-Paris, C. R., Gilger, M. A., Washington, M. K., Fan, K. H., Shyr, Y., Beauchamp, R. D. et al. (2013). Elevated ALCAM shedding in colorectal cancer correlates with poor patient outcome. *Cancer Res.* **73**, 2955–2964. doi:10.1158/0008-5472.CAN-12-2052
- Johannes, L., Wunder, C. and Shafaq-Zadah, M. (2016). Glycolipids and lectins in endocytic uptake processes. *J. Mol. Biol.* **428**, 4792–4818. doi:10.1016/j.jmb.2016.10.027
- Kahlert, C., Weber, H., Mogler, C., Bergmann, F., Schirmacher, P., Kenngott, H. G., Mattern, U., Mollberg, N., Rahbari, N. N., Hinz, U. et al. (2009). Increased expression of ALCAM/CD166 in pancreatic cancer is an independent prognostic marker for poor survival and early tumour relapse. *Br. J. Cancer* **101**, 457–464. doi:10.1038/sj.bjc.6605136
- Koivusalo, M., Welch, C., Hayashi, H., Scott, C. C., Kim, M., Alexander, T., Touret, N., Hahn, K. M. and Grinstein, S. (2010). Amiloride inhibits macropinosome formation by lowering submembranous pH and preventing Rac1 and Cdc42 signaling. *J. Cell Biol.* **188**, 547–563. doi:10.1083/jcb.200908086
- Kotelevets, L. and Chastre, E. (2020). Rac1 signaling: from intestinal homeostasis to colorectal cancer metastasis. *Cancers (Basel)* **12**, 665. doi:10.3390/cancers12030665
- Kumari, A., Pineau, J., Saez, P. J., Maurin, M., Lankar, D., San Roman, M., Hennig, K., Boura, V. F., Voituriez, R., Karlsson, M. C. I. et al. (2019). Actomyosin-driven force patterning controls endocytosis at the immune synapse. *Nat. Commun.* **10**, 2870. doi:10.1038/s41467-019-10751-7
- Lakshminarayan, R., Wunder, C., Becken, U., Howes, M. T., Benzing, C., Arumugam, S., Sales, S., Ariotti, N., Chambon, V., Lamaze, C. et al. (2014). Galectin-3 drives glycosphingolipid-dependent biogenesis of clathrin-independent carriers. *Nat. Cell Biol.* **16**, 595–606. doi:10.1038/ncb2970
- Leduc, C., Campas, O., Zeldovich, K. B., Roux, A., Jolimaître, P., Bourel-Bonnet, L., Goud, B., Joanny, J. F., Bassereau, P. and Prost, J. (2004). Cooperative extraction of membrane nanotubes by molecular motors. *Proc. Natl. Acad. Sci. USA* **101**, 17096–17101. doi:10.1073/pnas.0406598101
- Lee, J. C., Field, D. J. and Lee, L. L. (1980). Effects of nocodazole on structures of calf brain tubulin. *Biochemistry* **19**, 6209–6215. doi:10.1021/bi00567a041
- Loncar, A., Rincon, S. A., Lera Ramirez, M., Paoletti, A. and Tran, P. T. (2020). Kinesin-14 family proteins and microtubule dynamics define S. pombe mitotic and meiotic spindle assembly, and elongation. *J. Cell Sci.* **133**, jcs240234.
- Lugli, A., Iezzi, G., Hostettler, I., Muraro, M. G., Mele, V., Tornillo, L., Carafa, V., Spagnoli, G., Terracciano, L. and Zlobec, I. (2010). Prognostic impact of the expression of putative cancer stem cell markers CD133, CD166, CD44s, EpCAM, and ALDH1 in colorectal cancer. *Br. J. Cancer.* **103**, 382–390. doi:10.1038/sj.bjc.6605762
- Lundmark, R., Doherty, G. J., Howes, M. T., Cortese, K., Vallis, Y., Parton, R. G. and McMahon, H. T. (2008). The GTPase-activating protein GRAF1 regulates the CLIC/GEEC endocytic pathway. *Curr. Biol.* **18**, 1802–1808. doi:10.1016/j.cub.2008.10.044
- Maldonado-Baez, L., Cole, N. B., Kramer, H. and Donaldson, J. G. (2013). Microtubule-dependent endosomal sorting of clathrin-independent cargo by Hook1. *J. Cell Biol.* **201**, 233–247. doi:10.1083/jcb.201208172
- McIntosh, B. B., Pyrpasopoulos, S., Holzbaur, E. L. F. and Ostap, E. M. (2018). Opposing kinesin and myosin-i motors drive membrane deformation and tubulation along engineered cytoskeletal networks. *Curr. Biol.* **28**, 236–248.e235. doi:10.1016/j.cub.2017.12.007
- Minard, M. E., Herynk, M. H., Collard, J. G. and Gallick, G. E. (2005). The guanine nucleotide exchange factor Tiam1 increases colon carcinoma growth at metastatic sites in an orthotopic nude mouse model. *Oncogene* **24**, 2568–2573. doi:10.1038/sj.onc.1208503
- Minard, M. E., Ellis, L. M. and Gallick, G. E. (2006). Tiam1 regulates cell adhesion, migration and apoptosis in colon tumor cells. *Clin. Exp. Metastasis* **23**, 301–313. doi:10.1007/s10585-006-9040-z
- Miserey-Lenkei, S., Chalancon, G., Bardin, S., Formstecher, E., Goud, B. and Echard, A. (2010). Rab and actomyosin-dependent fission of transport vesicles at the Golgi complex. *Nat. Cell Biol.* **12**, 645–654. doi:10.1038/ncb2067
- Moore, O. L., Galletta, B. J. and Cooper, J. A. (2012). Roles for actin assembly in endocytosis. *Annu. Rev. Biochem.* **81**, 661–686. doi:10.1146/annurev-biochem-060910-094416
- Munsterberg, J., Loreth, D., Brylka, L., Werner, S., Karbanova, J., Gandrass, M., Schneegans, S., Besler, K., Hamester, F., Robador, J. R. et al. (2020). ALCAM contributes to brain metastasis formation in non-small-cell lung cancer through interaction with the vascular endothelium. *Neuro Oncol.* **22**, 955–966. doi:10.1093/neuonc/noaa028
- Nath, S., Bananis, E., Sarkar, S., Stockert, R. J., Sperry, A. O., Murray, J. W. and Wolkoff, A. W. (2007). Kif5B and Kifc1 interact and are required for motility and fission of early endocytic vesicles in mouse liver. *Mol. Biol. Cell* **18**, 1839–1849. doi:10.1091/mbc.e06-06-0524
- Nelissen, J. M., Peters, I. M., de Grooth, B. G., van Kooyk, Y. and Figdor, C. G. (2000). Dynamic regulation of activated leukocyte cell adhesion molecule-mediated homotypic cell adhesion through the actin cytoskeleton. *Mol. Biol. Cell* **11**, 2057–2068. doi:10.1091/mbc.11.6.2057
- Noda, Y., Okada, Y., Saito, N., Setou, M., Xu, Y., Zhang, Z. and Hirokawa, N. (2001). KIFC3, a microtubule minus end-directed motor for the apical transport of annexin XIIIb-associated Triton-insoluble membranes. *J. Cell Biol.* **155**, 77–88. doi:10.1083/jcb.200108042
- Nolen, B. J., Tomasevic, N., Russell, A., Pierce, D. W., Jia, Z., McCormick, C. D., Hartman, J., Sakowicz, R. and Pollard, T. D. (2009). Characterization of two classes of small molecule inhibitors of Arp2/3 complex. *Nature* **460**, 1031–1034. doi:10.1038/nature08231
- Ohneda, O., Ohneda, K., Arai, F., Lee, J., Miyamoto, T., Fukushima, Y., Dowbenko, D., Lasky, L. A. and Suda, T. (2001). ALCAM (CD166): its role in hematopoietic and endothelial development. *Blood* **98**, 2134–2142. doi:10.1182/blood.V98.7.2134
- Pollerberg, G. E., Thelen, K., Theiss, M. O. and Hochlehnert, B. C. (2013). The role of cell adhesion molecules for navigating axons: density matters. *Mech. Dev.* **130**, 359–372. doi:10.1016/j.mod.2012.11.002
- Poudel, K. R., Roh-Johnson, M., Su, A., Ho, T., Mathsyaraja, H., Anderson, S., Grady, W. M., Moens, C. B., Conacci-Sorrell, M., Eisenman, R. N. et al. (2018). Competition between TIAM1 and membranes balances Endophilin A3 activity in cancer metastasis. *Dev. Cell* **45**, 738–752.e736. doi:10.1016/j.devcel.2018.05.021
- Renard, H. F., Simunovic, M., Lemiere, J., Boucrot, E., Garcia-Castillo, M. D., Arumugam, S., Chambon, V., Lamaze, C., Wunder, C., Kenworthy, A. K. et al. (2015). Endophilin-A2 functions in membrane scission in clathrin-independent endocytosis. *Nature* **517**, 493–496. doi:10.1038/nature14064
- Renard, H. F., Tyckaert, F., Lo Giudice, C., Hirsch, T., Valades-Cruz, C. A., Lemaigre, C., Shafaq-Zadah, M., Wunder, C., Wattiez, R., Johannes, L. et al. (2020). Endophilin-A3 and Galectin-8 control the clathrin-independent endocytosis of CD166. *Nat. Commun.* **11**, 1457. doi:10.1038/s41467-020-15303-y
- Ribeiro, K. B., da Silva Zanetti, J., Ribeiro-Silva, A., Rapatoni, L., de Oliveira, H. F., da Cunha Tirapelli, D. P., Garcia, S. B., Feres, O., da Rocha, J. J. and Peria, F. M. (2016). KRAS mutation associated with CD44/CD166 immunorepression as predictors of worse outcome in metastatic colon cancer. *Cancer Biomark.* **16**, 513–521. doi:10.3233/CBM-160592
- Rossatti, P., Ziegler, L., Schregle, R., Betzler, V. M., Ecker, M. and Rossy, J. (2019). Cdc42 Couples T cell receptor endocytosis to GRAF1-mediated tubular invaginations of the plasma membrane. *Cells* **8**, 1388. doi:10.3390/cells8111388
- Sanders, A. J., Owen, S., Morgan, L. D., Ruge, F., Collins, R. J., Ye, L., Mason, M. D. and Jiang, W. G. (2019). Importance of activated leukocyte cell adhesion molecule (ALCAM) in prostate cancer progression and metastatic dissemination. *Oncotarget* **10**, 6362–6377. doi:10.18632/oncotarget.27279

- Sathe, M., Muthukrishnan, G., Rae, J., Disanza, A., Thattai, M., Scita, G., Parton, R. G. and Mayor, S.** (2018). Small GTPases and BAR domain proteins regulate branched actin polymerisation for clathrin and dynamin-independent endocytosis. *Nat. Commun.* **9**, 1835. doi:10.1038/s41467-018-03955-w
- Schliwa, M.** (1982). Action of cytochalasin D on cytoskeletal networks. *J. Cell Biol.* **92**, 79-91. doi:10.1083/jcb.92.1.79
- Serra-Marques, A., Martin, M., Katrukha, E. A., Grigoriev, I., Peeters, C. A., Liu, Q., Hooikaas, P. J., Yao, Y., Solianova, V., Smal, I. et al.** (2020). Concerted action of kinesins KIF5B and KIF13B promotes efficient secretory vesicle transport to microtubule plus ends. *Elife* **9**, e61302. doi:10.7554/eLife.61302
- Simunovic, M., Manneville, J. B., Renard, H. F., Evergren, E., Raghunathan, K., Bhatia, D., Kenworthy, A. K., Voth, G. A., Prost, J., McMahon, H. T. et al.** (2017). Friction mediates scission of tubular membranes scaffolded by BAR proteins. *Cell* **170**, 172-184.e111. doi:10.1016/j.cell.2017.05.047
- Soriano-Castell, D., Chavero, A., Rentero, C., Bosch, M., Vidal-Quadras, M., Pol, A., Enrich, C. and Tebar, F.** (2017). ROCK1 is a novel Rac1 effector to regulate tubular endocytic membrane formation during clathrin-independent endocytosis. *Sci. Rep.* **7**, 6866. doi:10.1038/s41598-017-07130-x
- Stephens, D. J.** (2012). Functional coupling of microtubules to membranes - implications for membrane structure and dynamics. *J. Cell Sci.* **125**, 2795-2804.
- Surviladze, Z. A., Waller, J. J., Strouse, C., Bologa, O., Ursu, V., Salas, J. F., Parkinson, G. K., Phillips, E., Romero, A., Wandinger-Ness, L. A. et al.** (2010). A potent and selective inhibitor of Cdc42 GTPase. In Probe Reports from the NIH Molecular Libraries Program, Bethesda, MD.
- Tudor, C., te Riet, J., Eich, C., Harkes, R., Smisdom, N., Bouhuijzen Wenger, J., Ameloot, M., Holt, M., Kanger, J. S., Figdor, C. G. et al.** (2014). Syntenin-1 and ezrin proteins link activated leukocyte cell adhesion molecule to the actin cytoskeleton. *J. Biol. Chem.* **289**, 13445-13460. doi:10.1074/jbc.M113.546754
- Wayt, J., Cartagena-Rivera, A., Dutta, D., Donaldson, J. G. and Waterman, C. M.** (2021). Myosin II isoforms promote internalization of spatially distinct clathrin-independent endocytosis cargoes through modulation of cortical tension downstream of ROCK2. *Mol. Biol. Cell* **32**, 226-236. doi:10.1091/mbc.E20-07-0480
- Williamson, C. D. and Donaldson, J. G.** (2019). Arf6, JIP3, and dynein shape and mediate macropinocytosis. *Mol. Biol. Cell* **30**, 1477-1489. doi:10.1091/mbc.E19-01-0022
- Willrodt, A. H., Salabarria, A. C., Schineis, P., Ignatova, D., Hunter, M. C., Vranova, M., Golding-Ochsenbein, A. M., Sigmund, E., Romagna, A., Strassberger, V. et al.** (2019). ALCAM mediates DC migration through afferent lymphatics and promotes allospecific immune reactions. *Front Immunol* **10**, 759. doi:10.3389/fimmu.2019.00759
- Xia, S., Lim, Y. B., Zhang, Z., Wang, Y., Zhang, S., Lim, C. T., Yim, E. K. F. and Kanchanawong, P.** (2019). Nanoscale architecture of the cortical actin cytoskeleton in embryonic stem cells. *Cell Rep* **28**, 1251-1267.e1257. doi:10.1016/j.celrep.2019.06.089
- Yang, W. X. and Sperry, A. O.** (2003). C-terminal kinesin motor KIFC1 participates in acrosome biogenesis and vesicle transport. *Biol. Reprod.* **69**, 1719-1729. doi:10.1095/biolreprod.102.014878
- Zhang, Y., Qian, C., Jing, L., Ren, J. and Guan, Y.** (2017). Meta-analysis indicating that high ALCAM expression predicts poor prognosis in colorectal cancer. *Oncotarget* **8**, 48272-48281. doi:10.18632/oncotarget.17707
- Zimmerman, A. W., Nelissen, J. M., van Emst-de Vries, S. E., Willems, P. H., de Lange, F., Collard, J. G., van Leeuwen, F. N. and Figdor, C. G.** (2004). Cytoskeletal restraints regulate homotypic ALCAM-mediated adhesion through PKC α independently of Rho-like GTPases. *J. Cell Sci.* **117**, 2841-2852. doi:10.1242/jcs.01139
- Zimmerman, A. W., Joosten, B., Torensma, R., Parnes, J. R., van Leeuwen, F. N. and Figdor, C. G.** (2006). Long-term engagement of CD6 and ALCAM is essential for T-cell proliferation induced by dendritic cells. *Blood* **107**, 3212-3220. doi:10.1182/blood-2005-09-3881